



Diurnal evolution of non-precipitating marine stratocumuli in an LES ensemble

Yao-Sheng Chen^{1,2}, Jianhao Zhang^{1,2}, Fabian Hoffmann³, Takanobu Yamaguchi^{1,2}, Franziska Glassmeier⁴, Xiaoli Zhou^{1,2}, and Graham Feingold²

¹Cooperative Institute for Research in Environmental Sciences, University of Colorado Boulder, Boulder, Colorado, USA

²NOAA Chemical Sciences Laboratory, Boulder, Colorado, USA

³Meteorologisches Institut, Ludwig-Maximilians-Universität München, Munich, Germany

⁴Delft University of Technology, Delft, Netherlands

Correspondence: Yao-Sheng Chen (yaosheng.chen@noaa.gov)

Abstract. We explore the impacts of the diurnal cycle, free-tropospheric (FT) humidity values, and interactive surface fluxes on the cloud system evolution of non-precipitating marine stratocumuli based on a large ensemble of large-eddy simulations. Cases are separated into three categories based on their degree of decoupling and cloud liquid water path (LWP_c). A new budget analysis method is proposed to analyze the evolution of LWP_c under both coupled and decoupled conditions. More coupled clouds start with relatively low LWP_c and cloud fraction (f_c) but experience the least decrease in LWP_c and f_c during the daytime. More decoupled clouds undergo greater daytime reduction in LWP_c and f_c , especially those with higher LWP_c at sunrise because they suffer from faster weakening of a net radiative cooling. During the nighttime, a positive correlation between FT humidity and LWP_c emerges, consistent with higher FT humidity reducing both radiative cooling and the humidity jump, both of which reduce entrainment and increase LWP_c . The time rate of change in the LWP_c is more likely to be negative for higher LWP_c and greater inversion base height (z_i), conditions under which entrainment dominates as turbulence develops. In the morning, the rate of the LWP_c reduction depends on the LWP_c at sunrise, z_i , and the degree of decoupling, with distinct contributions from subsidence and radiation. Under well-mixed conditions, it takes about 10 h for the surface fluxes to offset 15% of the changes in entrainment warming and drying, assuming no changes in transfer coefficients or surface wind speed.

1 Introduction

Subtropical marine stratocumuli cover vast areas of Earth's surface and play an important role in Earth's energy balance by reflecting solar radiation back to space. A cloud reflects more solar radiation when its liquid water is distributed amongst a larger number of aerosol particles to form more numerous and smaller cloud droplets (Twomey, 1974, 1977). This initial effect propagates to other cloud properties through a series of complex processes, e.g., suppression of precipitation formation (Albrecht, 1989; Pincus and Baker, 1994), enhancement of cloud-top entrainment (Bretherton et al., 2007; Wang et al., 2003), and an increase in solar absorption (Boers and Mitchell, 1994). These processes, all considered part of aerosol–cloud interactions (ACIs), may offset one another and their importance depends on the cloud's properties, its environment, and the time scale of interest (Stevens and Feingold, 2009).



From observations alone, it is difficult to identify and quantify the details of the aforementioned processes (e.g., Gryspeerdt et al., 2019; Wall et al., 2023), given the incomplete information of observed clouds and their environments, including co-
25 varying meteorology and aerosols, and often in the form of snapshots rather than temporal evolution of the same cloud field (Stevens and Feingold, 2009; Mülmenstüdt and Feingold, 2018). Despite recent efforts in inferring processes after constraining such co-variations (e.g., Zhang et al., 2022; Zhang and Feingold, 2023) and in quantifying the temporal evolution in the cloud responses to aerosol perturbations (e.g., Qiu et al., 2024; Smalley et al., 2024; Gryspeerdt et al., 2022), causality or process attribution remains a challenge. While opportunistic experiments, such as ship tracks, provide a way to observe the adjustment
30 of cloud properties to additional aerosol, they are often limited in their ability to represent the wide range of conditions the marine stratocumuli reside in (e.g., Manshausen et al., 2022; Yuan et al., 2023; Toll et al., 2019).

Meanwhile, fine-scale numerical modeling has been used to provide process-level understanding of ACIs. Early work focused primarily on case studies with aerosol perturbation experiments (Sandu et al., 2008; Caldwell and Bretherton, 2009; Wang and Feingold, 2009; Wang et al., 2010; Chen et al., 2011; Yamaguchi et al., 2015; Possner et al., 2018; Kazil et al., 2021; Prabhakaran et al., 2023; Chun et al., 2023). Although much has been learned from these studies, they do not cover the wide
35 range of real-world conditions.

Recent work by Feingold et al. (2016) and Glassmeier et al. (2019) took a different approach: exploring ACIs in large-eddy simulation (LES) ensembles of marine stratocumuli. They performed LESs of a large number of cases, each set up with different initial conditions specified by meteorological factors and aerosol number concentration. Instead of performing aerosol
40 perturbation experiments for each combination of meteorological factors, they used experiment design techniques to optimize the sampling of the initial condition space and later distilled the information regarding ACIs from both the individual and collective behaviors of ensemble members.

This approach has proved to be fruitful. Based on an LES ensemble of more than 150 nocturnal marine stratocumulus simulations, Glassmeier et al. (2019) found that several cloud properties (cloud fraction, cloud albedo, and relative cloud radiative effect) of ensemble members can be well described in the state-space of liquid water path (LWP) and cloud droplet number
45 concentration (N_d). Using the same LES ensemble, Hoffmann et al. (2020) showed that all non-precipitating cases in this ensemble approach a steady state LWP band from different parts of the state space: clouds starting with high LWP thin over time and clouds starting with low LWP, and possibly partial cloudiness, thicken over time. The authors further performed a budget analysis based on mixed-layer theory (MLT; Lilly, 1968) and demonstrated how the balance between radiative cooling, cloud-top entrainment warming and drying, and other processes shaped the N_d -dependence of steady state LWP. Glassmeier et al. (2021) estimated the magnitude and time scale of the LWP adjustment to an N_d perturbation from the collective behavior of the ensemble members and used them to infer biases in using ship-track to estimate the climatological forcing of anthropogenic aerosol. Hoffmann et al. (2023) explored the evolution of precipitating and non-precipitating stratocumuli in the space of albedo and cloud fraction using another ensemble of 127 cases.
50

The environmental conditions covered in the LES ensembles used by these works can be expanded. For instance, the free-troposphere (FT) in these simulations was fairly dry, while in reality a moister FT reduces cloud-top radiative cooling and modulates cloud-top entrainment warming and drying (Ackerman et al., 2004; Eastman and Wood, 2018). In addition, the



surface fluxes in those simulations were either constants prescribed following DYCOMS-II RF02 (Ackerman et al., 2009) or interactive but only responding to local wind fluctuations with calm mean winds, leading to relatively weak surface fluxes. Lastly, despite the insights gained from nocturnal simulations, the daytime behavior of marine stratocumulus population needs to be explored to understand the shortwave radiative effects of these clouds, which are more relevant to aerosol–cloud climate forcing and issues like marine cloud brightening (Latham, 1990; Feingold et al., 2024).

In this study, we explore the impacts of diurnal cycles, FT humidity values, and interactive surface fluxes on the cloud system evolution. The rest of this manuscript is organized as follows. We first introduce the model and simulation configurations in Section 2 and then provide an overview of the LES ensemble in Section 3. Next, we introduce a new budget analysis method and present results in Section 4. With this method, we examine the nighttime and daytime evolution of individual cases in Section 5. A few specific issues will be discussed in Section 6, after which we end the paper with a summary in Section 7.

2 Model and simulations

All LESs for this study are performed using the System for Atmospheric Modeling (SAM; Khairoutdinov and Randall, 2003), version 6.10.10. SAM solves the anelastic Navier-Stokes equations in finite difference representation for the atmosphere on the Arakawa C grid. Similar to recent work by Yamaguchi et al. (2017) and Glassmeier et al. (2019), SAM is configured with a fifth-order advection scheme by Yamaguchi et al. (2011) and Euler time integration scheme for scalars, a second-order center advection scheme and with the third-order Adams-Bashforth time integration scheme for momentum, a 1.5-order TKE-based subgrid model similar to Deardorff (1980), a bin-emulating bulk two-moment microphysics parameterization (Feingold et al., 1998) assuming a log-normal aerosol size distribution with fixed size and width parameters, and the Rapid Radiative Transfer Model (RRTMG; Mlawer et al., 1997; Iacono et al., 2008) that is modified to take into account background profiles of temperature and moisture above the model domain top (Yamaguchi et al., 2015), which is critical for radiative transfer in shallow domain simulations.

Different from Yamaguchi et al. (2017) and Glassmeier et al. (2019), the SAM used for this work uses the total water mixing ratio (sum of vapor and hydrometeors) and the total number concentration (sum of aerosol and drop number concentrations) as prognostic variables to ensure better closure of the budgets associated with these two quantities for advection and several other physical processes. As a result, the water vapor mixing ratio is diagnosed from the total water and hydrometeor mixing ratios and the aerosol number concentration is diagnosed from the total, cloud droplet, and rain drop number concentrations. See details in the last paragraph of Section 2 in Yamaguchi et al. (2019).

As in Feingold et al. (2016) and Glassmeier et al. (2019), the LES ensemble members are generated from perturbed initial conditions. The initial profiles of liquid water potential temperature (θ_l) and total water mixing ratio (q_t) are each constructed from two parts: a well-mixed boundary layer (BL) profile including a sharp jump at the top of the BL and a FT profile based on ERA5 climatology (Hersbach et al., 2020) and the Marine ARM GPCI Investigation of Clouds (MAGIC) campaign (Lewis et al., 2012; Zhou et al., 2015) observations. The initial BL θ_l and q_t profiles are controlled by five parameters: θ_l and q_t in the BL and their jumps, $\Delta\theta_l$ and Δq_t , across the inversion base at the height of h_{mix} . See Appendix A for details on the FT profiles



and the construction of the complete profiles. The initial aerosol number mixing ratio, specified by a sixth parameter, N_a , is uniform throughout the domain. The initial horizontal wind speed is 0 m s^{-1} everywhere.

Hundreds of initial profiles are set up from sets of these six parameters randomly and independently drawn from their ranges: BL θ_l is drawn from 284 to 294 K, BL q_t from 6.5 to 10.5 g kg^{-1} , $\Delta\theta_l$ from 6 to 10 K, Δq_t from -10 to 0 g kg^{-1} , h_{mix} from 95 500 to 1300 m, and N_a from 30 to 500 mg^{-1} . Compared with the parameter ranges used in Glassmeier et al. (2019), the range for Δq_t now covers -6 to 0 g kg^{-1} to include conditions with more humid FT. All initial profiles with (1) height of lifted condensation level (z_{LCL}) between around 225 m and 1075 m, (2) a saturated layer (i.e., $h_{\text{mix}} > z_{\text{LCL}}$), and (3) FT θ_l and q_t profiles falling between the minimum and maximum of the ERA5 climatological profiles are simulated with the lower boundary conditions and large-scale forcings described below, which are the same for all simulations.

100 First, the surface fluxes of sensible heat, latent heat, and momentum are computed based on Monin-Obukhov similarity. The sea surface temperature (SST) is fixed for all simulations at 292.4 K. Since the mean horizontal wind speed is close to 0 m s^{-1} in the lowest model level as a result of the simulation setup, a constant horizontal wind speed of 7 m s^{-1} is added to the surface local wind fluctuation when calculating sensible and latent heat fluxes to obtain realistic flux values. Both this wind speed and the SST are based on the ERA5 climatology from the same region and time period as described in Appendix A.
105 Second, a constant surface aerosol flux of $70 \text{ cm}^{-2} \text{ s}^{-1}$, based on estimates by Kazil et al. (2011), is prescribed to offset the loss of aerosols through coalescence scavenging (Wang et al., 2010). Lastly, a time-invariant subsidence profile is imposed as

$$w_s = \begin{cases} -Dz, & z < 2000 \text{ m} \\ -0.0075 \text{ m s}^{-1}, & z \geq 2000 \text{ m}, \end{cases} \quad (1)$$

where the divergence $D = 3.75 \times 10^{-6} \text{ s}^{-1}$. No other large-scale forcing is present in the simulations.

The simulation domain is $48 \times 48 \times 2.5 \text{ km}^3$ in the x-, y-, and z-dimensions with 200-m horizontal and 10-m vertical grid 110 spacings. It uses periodic lateral boundary conditions and has a damping layer from 2 km to domain top. All simulations are initialized at 18:40 local time (LT; 03:00Z) and then advanced for 24 h with a 1-s time step. Sunrise occurs between 05:23 and 05:24 LT and sunset occurs between 18:36 and 18:37 LT.

For this study, we focus on non-precipitating cases, defined by a cloud-base precipitation rate of less than 0.5 mm day^{-1} (Wood, 2012). We further exclude simulations with multi-layer clouds, including surface fog. Finally, we discard simulations 115 where the cloud top ever reaches 2 km, the lower bound of the damping layer, to avoid unrealistic results. This leaves 245 cases for further investigation. The first 2-h of each simulation is excluded as the spin-up.

3 Overview of LES ensemble behavior

In this section, we present an overview of the evolution of the 245 non-precipitating cases in our LES ensemble. Following Glassmeier et al. (2019), we start with the trajectories in the plane of cloud droplet number concentration (N_d) and cloud liquid 120 water path (LWP_c), both based on columns with cloud optical depth greater than 1, the definition of “cloudy column” in this work (Figure 1). During the nighttime, the cases that start with low LWP_c experience an increase in LWP_c , while the behavior



of the high LWP_c cases is not immediately clear. The nighttime cloud fractions (f_c) are usually high. At sunrise, 68% of cases have $f_c > 0.99$ and 86% cases have $f_c > 0.95$. During the daytime, all cases start to lose LWP_c and f_c right after sunrise or in the early morning. Between noon and 15:00, about 86% cases reach their lowest daytime LWP_c . In the last hour of the simulation, 94% cases are gaining LWP_c . Very low f_c occurs for many cases in the afternoon.

3.1 Categorization of cases

To provide a more consolidated view of the evolution, we categorize the cases by their degree of decoupling in the morning because the diurnal decoupling (Nicholls, 1984; Turton and Nicholls, 1987) is a common feature of the cloud-topped marine BL diurnal cycle and we expect different diurnal cycles between more coupled and more decoupled cases. We compute the relative decoupling index (denoted with \mathcal{D}) defined by Kazil et al. (2017),

$$\mathcal{D} = \frac{\overline{z_{cb}} - \overline{z_{LCL}}}{\overline{z_{LCL}}}, \quad (2)$$

where $\overline{z_{cb}}$ and $\overline{z_{LCL}}$ are the mean cloud base height and mean lifting condensation level (LCL, determined from conditions in the lowest model level), both averaged for cloudy columns. This index is a variant of the subcloud decoupling index, $\overline{z_{cb}} - \overline{z_{LCL}}$, originally proposed by Jones et al. (2011). A small value of \mathcal{D} is more likely to be coupled while a large value of \mathcal{D} is more decoupled.

Figure 2a shows \mathcal{D} at 09:40 LT in the plane of LWP_c and domain-mean inversion base height (z_i , based on levels with the greatest vertical gradient of liquid water static energy in individual columns) at sunrise. Clouds with greater \mathcal{D} tend to occur in deeper BLs; many of these clouds experience very low daytime f_c minima (Figure 2b) unless they start with very high LWP_c at sunrise, although most cases have daytime f_c maxima that are close to overcast (not shown). Based on this finding, we divide the cases into three categories based on \mathcal{D} at 09:40 and LWP_c at sunrise (05:22): (1) loDloL ($\mathcal{D} \leq 1$), (2) hiDloL ($\mathcal{D} > 1$ and $LWP_c \leq 180 \text{ g m}^{-2}$, the highest LWP_c for the loDloL category), and (3) hiDhiL ($\mathcal{D} > 1$ and $LWP_c > 180 \text{ g m}^{-2}$) for further analysis (Figure 2c). Figure 2d shows the time series of \mathcal{D} by category. During the nighttime, the medians of \mathcal{D} for all three categories are relatively small, suggesting more coupled conditions. Some cases in the hiDloL and hiDhiL categories always exhibit a higher degree of decoupling during the night. During the daytime, \mathcal{D} for all three categories increases into the afternoon. Overall, cases in the loDloL category experience weaker decoupling with their \mathcal{D} start to increase at a slower rate from a later time, compared with other two categories. Figure 2e shows the time series of median $\overline{z_{cb}}$ and median $\overline{z_{LCL}}$ by category. During the daytime, the median $\overline{z_{LCL}}$ decreases for both hiDloL and hiDhiL, consistent with a strengthening decoupling limiting the surface based mixed layer. This does not happen to loDloL. Also, both hiDloL and hiDhiL categories experience dramatic diurnal changes in median $\overline{z_{cb}}$ and the cloud depth, approximated with $z_i - \overline{z_{cb}}$. Even though the categorization is based on \mathcal{D} , it nicely separates the loDloL category from the other two categories through the daytime.

3.2 Cloud evolution by category

Figures 3a and 3b display the average time series of LWP_c and f_c for three categories. Among the three categories, the loDloL category shows the lowest nighttime LWP_c and f_c . However, this category also has the smallest decrease in LWP_c and f_c



during the day. By contrast, the hiDloL category has greater LWP_c and nearly overcast conditions ($f_c > 0.99$) at sunrise but
155 experiences a much more dramatic decrease in both LWP_c and f_c . The hiDhiL category has the highest LWP_c and f_c at sunrise
among all three categories. This category also shows diurnal fluctuations of large amplitude in both LWP_c and f_c with the
daytime minimum between the loDloL and hiDloL categories for both variables. It reaches its lowest LWP_c and lowest f_c
latest in the day among all three categories. At the end of the simulation, all three categories experience a recovery of both
160 LWP_c and f_c . At this stage, they all have similar LWP_c , indicating that the diurnal cycle imposes a strong constraint to narrow
the range of LWP_c . In contrast, the f_c differs significantly: the loDloL category has the highest f_c and the hiDloL category
the lowest f_c .

There is hysteresis in the mean trajectories of the three categories in the plane of f_c and the cloud depth ($z_i - z_{cb}$) plane (Figure
3c). The trajectory of the loDloL category makes the smallest loop, which can be interpreted as the least diurnal variation in
cloud aspect ratio (the ratio between the cloud depth and f_c). Clouds in the hiDloL and hiDhiL categories experience greater
165 variation in the aspect ratio, more so for the hiDloL categories. We examine the 3-D cloud fields for selected cases from these
two categories and find that clouds in both categories evolve into a cumulus-rising-into-stratocumulus structure by noon (not
shown). The cloud bases of the cumuli lower slightly while the stratocumuli continue to thin and lose f_c . This transition lowers
 $\overline{z_{cb}}$ and leads to the segments in the trajectories where f_c decreases but cloud depth starts to recover. As the clouds develop
towards sunset, they regain f_c to become stratiform again.

170 3.3 Surface fluxes

To end this overview, we examine the surface fluxes in the simulations (Figures 4a and 4b). At the end of the first 2-h of the
simulations, both the ranges of surface sensible heat flux (SHF) and latent heat flux (LHF) from all simulations encompass
the values prescribed in the DYCOMS-II RF02 case (i.e., 16 and 93 $W m^{-2}$, respectively). Afterwards, the SHF decreases
over time until late afternoon as the SHF effectively brings the BL air temperature towards the SST (Figures 4a). The SHF is
175 the strongest in the loDloL category, followed by the hiDhiL and then the hiDloL categories. This is because the shallower
BLs in our ensemble also tend to be colder due to the criteria applied in the initial profiles. (For example, for a shallow BL to
be initially saturated, its z_{LCL} needs to be lower, which is more likely when the initial BL θ_1 is low. See more in Section 2.)
LHF shows a smaller relative change throughout the day (Figures 4b). During the nighttime, the LHF for the loDloL category
remains quite steady and that for the hiDloL category even increases as the turbulence spins up. The LHF is also the strongest
180 in the loDloL category, while the LHF from the other two categories are comparable at all times.

Following Eq. 1 in Lilly (1968), the domain-mean surface sensible and latent heat fluxes (SHF and LHF) can be written as

$$SHF = C_T U (\theta_{SST} - \theta_{air}), LHF = C_q U (q_{sat}(SST) - q_{v,air}), \quad (3)$$

where the wind speed used for surface flux calculations (U), lowest model level air temperature and water vapor mixing ratio
(θ_{air} and $q_{v,air}$) are also the domain-means. Recall that in our simulations, the SST is 292.4 K and equivalent to a potential
185 temperature, θ_{SST} , of 290.9 K given the surface pressure used in the simulations. (See Appendix.) The saturation mixing ratio
at SST ($q_{sat}(SST)$) is approximately constant due to the negligible drift of surface pressure. Comparing Figures 4c–f with



Figures 4a–b, it is clear that the evolutions of the SHF and LHF in our simulations are driven primarily by $(\theta_{\text{SST}} - \theta_{\text{air}})$ and $(q_{\text{sat}}(\text{SST}) - q_{\text{v,air}})$, respectively. On average, the transfer coefficients for SHF (C_T) and for LHF (C_q) that are diagnosed from Eq. (3) decrease slightly over time, although cases with θ_{air} very close to θ_{SST} see larger fluctuations in C_T . U mostly ranges
190 between 7 than 7.3 m s^{-1} throughout the day (Figure S1) because they result from the summation of relatively weak local wind velocities and a large constant wind speed (7 m s^{-1} , see Section 2). Our results are consistent with the findings reported by Kazil et al. (2014) for a closed-cell stratocumulus case.

4 Budget analysis for evolution of LWP_c

We perform a detailed budget analysis to understand the simulated LWP_c evolution. Previous studies used mixed-layer theory
195 (MLT) to calculate the LWP_c tendency from the tendencies of BL mean liquid water potential temperature (θ_l) and total water mixing ratio (q_t) as well as the motion of z_i (Wood, 2007; Caldwell and Bretherton, 2009; van der Dussen et al., 2014; Ghonima et al., 2015; Hoffmann et al., 2020). It is well-known that MLT is not applicable to the decoupled BL, which is prevalent in our simulations during the daytime. Here, we apply the MLT-based approach to both the BL and the “cloud volume” (CV), which we define for a given time t as the volume consisting of all cloudy columns between $z_i(t)$ and the first grid box interface
200 below \bar{z}_{cb} (Figure S2). The choice of this volume is inspired by previous work showing success in assuming the cloud layer being well-mixed under decoupled conditions (Turton and Nicholls, 1987; Bretherton and Wyant, 1997). It is also based on our observation that in our simulations the entrainment velocity, diagnosed as

$$w_e = \frac{dz_i}{dt} - w_s(z_i), \quad (4)$$

is rarely negative, even at its weakest point in the late afternoon, meaning there is always some turbulent motion near the cloud
205 top that mixes the air between the cloud layer and the FT. Different from previous work, we further focus on the cloudy region of the cloud layer. The specific definition of the CV base takes full advantage of quantities reported by SAM at the grid box interface to reduce the impacts of vertical interpolation. The CV depth defined this way is within a few percent of the actual cloud depth. We first show the derivation of CV budgets and then show results from both the BL and CV budgets.

4.1 Derivation

210 Consider a scalar quantity ϕ (in our case θ_l or q_t) at time t in a volume consisting of a set of model columns covering a fraction of the domain area (f) between the volume base height $z_0(t)$ and $z_i(t)$. We denote the total amount of this scalar quantity and air mass in this volume with Φ and M , respectively. Since SAM solves the anelastic equations of motion, where the air density ρ_0 only changes with height,

$$\Phi = f(t) \int_{z_0(t)}^{z_i(t)} \rho_0(z) \phi(z, t) dz, \quad (5)$$



215 and

$$M = f(t) \int_{z_0(t)}^{z_i(t)} \rho_0(z) dz = \langle \rho_0 \rangle f(t) h(t), \quad (6)$$

where $\langle \rho_0 \rangle$ is the mean air density of the volume, $\phi(z, t)$ is the time-dependent mean ϕ profile, and $h(t) = z_i(t) - z_0(t)$ is the volume thickness. The mean scalar quantity in this volume is

$$\langle \phi \rangle = \Phi / M. \quad (7)$$

220 Inspired by the derivation in Appendix B in Kazil et al. (2016), we build a budget for $\langle \phi \rangle$ from the budgets for Φ and M via

$$\frac{d\langle \phi \rangle}{dt} = \frac{1}{M} \frac{d\Phi}{dt} - \frac{\langle \phi \rangle}{M} \frac{dM}{dt}. \quad (8)$$

The $\langle \phi \rangle$ tendency can also be decomposed into the contributions from various processes

$$\frac{d\langle \phi \rangle}{dt} = \sum_P \left. \frac{d\langle \phi \rangle}{dt} \right|_P = \sum_P \left(\left. \frac{1}{M} \frac{d\Phi}{dt} \right|_P - \left. \frac{\langle \phi \rangle}{M} \frac{dM}{dt} \right|_P \right), \quad (9)$$

where the processes P include volume-top entrainment (ENTR), processes at volume sides (LAT for lateral), radiation (RAD),
 225 subsidence (SUBS), and processes at the volume base: transport flux at volume base (BASE), precipitation flux at volume base (PRCP), and a term tracking the impacts of the rising or lowering of the volume base (BM, standing for “base motion”). The $d\langle \phi \rangle / dt$ due to each of these seven processes can be calculated from $d\Phi / dt$ and dM / dt due to the same process via Eq. (9).

When we apply this approach to the budget of $\langle \phi \rangle$ in a CV, f is equivalent to cloud fraction f_c and several terms are quite straightforward to estimate accurately. The RAD and BASE terms for Φ are directly computed from the 3-D modeled fields of
 230 radiative heating rate, vertical velocity, and ϕ , and neither process modifies M . Although we are dealing with non-precipitating cases, we retain the PRCP terms to minimize the residual. The BM term is calculated following

$$\left. \frac{d\langle \phi \rangle}{dt} \right|_{\text{BM}} = \left. \frac{1}{M} \frac{d\Phi}{dt} \right|_{\text{BM}} - \left. \frac{\langle \phi \rangle}{M} \frac{dM}{dt} \right|_{\text{BM}} = - \frac{\rho_0(z_0) \phi(z_0, t) f_c}{M} \frac{dz_0}{dt} + \frac{\rho_0(z_0) \langle \phi \rangle f_c}{M} \frac{dz_0}{dt}. \quad (10)$$

The SUBS term for Φ is diagnosed by applying the Reynolds Transport Theorem (RTT),

$$\begin{aligned} \left. \frac{d\Phi}{dt} \right|_{\text{SUBS}} &= f_c \int_{z_0(t)}^{z_i(t)} \rho_0(z) \left. \frac{d\phi(z, t)}{dt} \right|_{\text{SUBS}} dz + \rho_0(z_i) \phi(z_i, t) f_c \left. \frac{dz_i}{dt} \right|_{\text{SUBS}} \\ &= f_c \int_{z_0(t)}^{z_i(t)} \rho_0(z) \left. \frac{d\phi(z, t)}{dt} \right|_{\text{SUBS}} dz + \rho_0(z_i) \phi(z_i, t) f_c w_s(z_i), \end{aligned} \quad (11)$$

where $d\phi(z, t) / dt|_{\text{SUBS}}$ is calculated by applying SAM’s subsidence subroutine to the $\phi(z, t)$ profile. Note that although the CV base is defined to be close to \bar{z}_{cb} , which evolves due to many processes, this choice of CV base is to avoid applying MLT later to deeper stratified layers. In other words, as long as the CV base sits in a well-mixed layer, there is no need to update



its height based on the cloud base height, and our choice to move it following the cloud base height is arbitrary. So, physical
 240 processes do not directly move the CV base and there is no $dz_0(t)/dt$ in the terms for any processes but the BM term. The
 SUBS term for M is

$$\left. \frac{dM}{dt} \right|_{\text{SUBS}} = \rho_0(z_i) f_c w_s(z_i). \quad (12)$$

The ENTR flux of Φ can be parameterized as

$$\left. \frac{d\Phi}{dt} \right|_{\text{ENTR}} = \rho_{0,e} \phi_e(t) f_c w_e, \quad (13)$$

245 where w_e is the entrainment velocity estimated from Eq. (4) and $\rho_{0,e}$ and $\phi_e(t)$ are an air density and a ϕ value that are relevant
 to the entrainment flux of ϕ . (Subscript “e” stands for “entrainment”, as in w_e .) Combined with the ENTR term for M , the
 contribution of entrainment to the $\langle \phi \rangle$ tendency is

$$\left. \frac{d\langle \phi \rangle}{dt} \right|_{\text{ENTR}} = \frac{1}{M} \left. \frac{d\Phi}{dt} \right|_{\text{ENTR}} - \frac{\langle \phi \rangle}{M} \left. \frac{dM}{dt} \right|_{\text{ENTR}} = \frac{\rho_{0,e} \phi_e(t) f_c w_e}{M} - \frac{\rho_0(z_i) \langle \phi \rangle f_c w_e}{M}. \quad (14)$$

Assuming constant ρ_0 and overcast conditions ($f_c = 1$), Eq. (14) reduces to

$$250 \left. \frac{d\langle \phi \rangle}{dt} \right|_{\text{ENTR}} = \frac{1}{h} w_e \Delta \phi, \quad (15)$$

where $\Delta \phi$ is the ϕ jump at the volume top. Previous work used ϕ values at certain levels above and below z_i (usually denoted
 as z_+ and z_-) to calculate the jump (Yamaguchi et al., 2011; Bretherton et al., 2013). Comparing Eqs. (14) and (15), it seems
 that we can follow a similar method to find a level above z_i and use the ϕ and ρ_0 at this level in place of ϕ_e and $\rho_{0,e}$. However,
 it is unclear what formula can be used to reliably find this level for all coupled and decoupled conditions in our simulations.

255 With Eq. (14), the challenging part is the entrainment flux term, $d\Phi/dt|_{\text{ENTR}}$. For now, we approximate it with the entrainment
 flux term for the BL. We first apply Eq. (9) to the whole BL. In this case, the BM and LAT terms vanish and the BASE term is
 calculated from the surface fluxes reported by SAM (denoted with SURF term). Because all terms other than the ENTR term
 are relatively easy to estimate directly and accurately, we don't keep a residual term, essentially lumping any residual into the
 ENTR term. So,

$$260 \left. \frac{d\langle \phi \rangle_{\text{BL}}}{dt} \right|_{\text{ENTR}} = \frac{d\langle \phi \rangle_{\text{BL}}}{dt} - \left(\left. \frac{d\langle \phi \rangle_{\text{BL}}}{dt} \right|_{\text{RAD}} + \left. \frac{d\langle \phi \rangle_{\text{BL}}}{dt} \right|_{\text{SUBS}} + \left. \frac{d\langle \phi \rangle_{\text{BL}}}{dt} \right|_{\text{SURF}} + \left. \frac{d\langle \phi \rangle_{\text{BL}}}{dt} \right|_{\text{PRCP}} \right). \quad (16)$$

Then,

$$\left. \frac{d\Phi_{\text{BL}}}{dt} \right|_{\text{ENTR}} = \langle \phi \rangle_{\text{BL}} \left. \frac{dM_{\text{BL}}}{dt} \right|_{\text{ENTR}} + M_{\text{BL}} \left. \frac{d\langle \phi \rangle_{\text{BL}}}{dt} \right|_{\text{ENTR}} = \rho_0(z_i) \langle \phi \rangle_{\text{BL}} w_e + M_{\text{BL}} \left. \frac{d\langle \phi \rangle_{\text{BL}}}{dt} \right|_{\text{ENTR}}. \quad (17)$$

We use this term in place of $d\Phi/dt|_{\text{ENTR}}$ in the CV budget.

Regarding the LAT term, we can write

$$265 \left. \frac{\langle \phi \rangle}{M} \frac{dM}{dt} \right|_{\text{LAT}} = \frac{\langle \phi \rangle h(t) \langle \rho_0 \rangle}{M} \frac{df_c}{dt} = \frac{\langle \phi \rangle}{f} \frac{df_c}{dt}. \quad (18)$$



Finally, we attribute all the remaining $\langle \phi \rangle$ tendency to $d\Phi/dt|_{LAT}$ to close the budget without the need for a residual term.

Thus far, we have been tracking the budget of $\langle \theta_1 \rangle$ and $\langle q_t \rangle$ and have not invoked MLT. Next, we apply the following equation for the LWP_c tendency, derived based on MLT, to the CV,

$$\frac{dLWP_c}{dt} = \Gamma_1 \langle \rho_0 \rangle (z_i - z_{cb}) \left[\frac{dz_i}{dt} - \left(\frac{dz_{cb}}{d\langle q_t \rangle} \frac{d\langle q_t \rangle}{dt} + \frac{dz_{cb}}{d\langle \theta_1 \rangle} \frac{d\langle \theta_1 \rangle}{dt} \right) \right], \quad (19)$$

270 where z_{cb} is the mean cloud base height, Γ_1 is the liquid water adiabatic lapse rate, and $dz_{cb}/d\langle \theta_1 \rangle$ and $dz_{cb}/d\langle q_t \rangle$ are based on the derivation in Ghonima et al. (2015) and follow similar notations in Hoffmann et al. (2020). In the calculation of Γ_1 , $dz_{cb}/d\langle \theta_1 \rangle$, and $dz_{cb}/d\langle q_t \rangle$, the actual cloud base air temperature and pressure are used. We decompose dz_i/dt into the sum of w_e and w_s , substitute $d\langle q_t \rangle/dt$ and $d\langle \theta_1 \rangle/dt$ with the sum of individual budget terms diagnosed earlier, and finally group the dz_i/dt , $d\langle q_t \rangle/dt$, and $d\langle \theta_1 \rangle/dt$ terms on the right-hand side of Eq. (19) by processes. Budget terms are diagnosed at the end of
275 each simulation hour (local time 40 min past each hour)

4.2 Diurnal cycles of BL budgets

We briefly introduce the diurnal cycles of the BL $\langle \theta_1 \rangle$ and $\langle q_t \rangle$ budgets and the LWP_c budget when they are used in Eq. (19) to provide a reference for the CV budgets in the next subsection.

The BL $\langle \theta_1 \rangle$ and $\langle q_t \rangle$ budgets share similarity between the three categories, i.e., loDloL, hiDloL, and hiDhiL (Figure 5).
280 For the BL $\langle \theta_1 \rangle$ budget (left column in Figure 5), RAD and ENTR are the leading terms during the nighttime. After sunrise, RAD quickly changes from cooling to warming, while ENTR warming weakens at a slower rate, leading to a peak in positive net BL $\langle \theta_1 \rangle$ tendency in the morning. For the BL $\langle q_t \rangle$ budget (right column Figure 5), ENTR and SURF are the leading terms throughout the day. After sunrise, ENTR drying weakens faster than SURF moistening, leading to a peak in positive net BL $\langle q_t \rangle$ tendency between noon and 15:00 LT. Recall that in MLT, the subsidence has zero contributions to the tendencies of both
285 the mixed-layer $\langle \theta_1 \rangle$ and mean $\langle q_t \rangle$. In our case, the contributions are not zero but still small compared with leading terms.

Figure 6 shows the LWP_c budgets when the BL $\langle \theta_1 \rangle$ and $\langle q_t \rangle$ budgets are used in Eq. (19). Comparing the actual LWP_c tendency and the residual in the right column of Figure 6, applying MLT to the BL achieves fairly good closure during the nighttime for the loDloL category and between 02:00 and sunrise for the hiDloL category; the residual continues to grow between 23:00 and sunrise for the hiDhiL category. During the daytime, the residual is unacceptably large, demonstrating that
290 applying the MLT-based LWP_c budget analysis to the BL is no longer appropriate.

The left column in Figure 6 shows the actual LWP_c tendency as well as the contributions from the RAD, ENTR, SUBS, and SURF terms. During the nighttime, the most distinct feature is that the SUBS term is much more important relative to other terms in the LWP_c budget than in the BL $\langle \theta_1 \rangle$ and $\langle q_t \rangle$ budgets. This is due to the strong negative contribution by the subsidence to the dz_i/dt term in Eq. (19). It is more negative for the hiDloL and hiDhiL categories because cases in these two categories
295 have a higher z_i and thus a stronger subsidence due to the subsidence profile we impose. The ENTR term is comparable to other terms because its strong warming and drying effect (Figure 5) is offset by its positive contribution to the dz_i/dt term. We do not discuss the results for the daytime due to the large residual.



4.3 Diurnal cycles of CV budgets

We first present the diurnal cycles of CV $\langle\theta_1\rangle$ and $\langle q_t\rangle$ budgets averaged by category (Figure 7). Similar to the BL budgets, the ENTR and RAD terms are the leading terms for the CV $\langle\theta_1\rangle$ budget during the nighttime. Both weaken after sunrise, with RAD cooling weakening faster. The ENTR warming decreases steadily towards late afternoon and becomes stronger before sunset. The main difference from the BL budgets in the left column of Figure 5 is that RAD is mostly cooling during the daytime because much of the warming effect by RAD occurs in the subcloud layer and is excluded in the CV $\langle\theta_1\rangle$ budget. This warming strengthens the stratification of the subcloud layer, weakens the turbulent motion, and limits its impacts on the CV. The remaining effects of this subcloud warming on the CV are accounted as transport in BASE and LAT terms. The RAD cooling becomes stronger after around 09:00 or 10:00. It continues to strengthen through the rest of the day for the loDloL and hiDhiL categories, even though the LWP_c does not recover until afternoon (Figure 3a). This trend is dominated by the trend in CV-integrated radiative heating rates (not shown). For the hiDloL category, there is a second weakening-strengthening cycle. This is a signature of the rapid lowering of $\overline{z_{cb}}$ in this category as the stratiform parts of the clouds shrink and cumulus parts dominate (see Section 3 and Figure 2e) and, as a result, the total radiative divergence for the CV is distributed over a deeper layer. Note that due to subsidence and the growing of z_i , the FT in all our simulations becomes drier over time. (FT q_t values at the end of the simulations are between 64% and 85% of those at sunrise.) This effect likely also modulates the balance between longwave cooling and shortwave absorption.

As the ENTR term for the CV $\langle\theta_1\rangle$ continues to decrease after the radiation passes its morning weakest point, the BASE-n-LAT term starts to play a more significant role (left column in Figure 7). This term is defined as the sum of the BASE and LAT terms. It represents the processes associated with the interface between the CV and the rest of the BL (i.e., CV base and lateral sides). It shows an opposite trend from the RAD term and becomes the main term balancing the radiation in the afternoon. This can be interpreted as follows: while there is not enough kinetic energy for mixing across the inversion base, the radiative cooling in the CV still couples with the dynamics inside the BL.

For $\langle q_t\rangle$, the ENTR and BASE-n-LAT terms are the leading terms (right column of Figure 7). Unlike the BASE-n-LAT term for the $\langle\theta_1\rangle$ budget, which can warm or cool the CV at different times, the BASE-n-LAT term mostly moistens the CV.

As mentioned before, the base motion (BM) term comes from the arbitrary choice of CV base height, although it is related to the actual cloud base height evolution. When the BL is stratified, a rising CV base means the air mass near cloud base, which has lower θ_1 than the CV mean, is excluded from the CV. This results in an increase in $\langle\theta_1\rangle$ in the CV. Similarly we can infer the sign of this term for $\langle\theta_1\rangle$ and $\langle q_t\rangle$ budgets under other conditions. This BM term is near zero during the nighttime when the BL is close to being well-mixed. Its relative importance peaks between 13:00 and 15:00 for both $\langle\theta_1\rangle$ and $\langle q_t\rangle$ when the cloud base averaged for all cases starts to lower, accompanying the recovery of LWP_c . The magnitudes of cooling and moistening during this time are greater than the magnitudes of warming and drying between 09:00 and noon, primarily because the layer near the cloud base is more stratified in the afternoon.

The SUBS term always warms and dries the CV. Its effect peaks in the early afternoon around the time when the clouds are the thinnest.



4.4 Diurnal cycles of the LWP_c budget

Figure 8 shows the LWP_c budget by category, with the actual LWP_c tendency and ENTR, RAD, SUBS, and BASE-n-LAT terms in the left column and the BM and residual terms in the right column. The PRCP terms are negligible and omitted.

335 We start with the terms in the right column. For all three categories, it is encouraging that the residual in the LWP_c budget is fairly small. The improvement over the results based on the BL budgets (Figure 6) is dramatic for all three categories between sunrise and early afternoon; it is also evident for the hiDhiL category during the nighttime. Although the BM term is overall not important until early afternoon, quantifying it for CV $\langle\theta_1\rangle$ and $\langle q_1\rangle$ budgets makes the LAT term (and thus the BASE-n-LAT term) slightly more accurate. Interestingly, the sum of the residual and BM term is even closer to zero. Qualitatively, the
340 correlation between the BM term and the residual is expected considering that more stratified conditions simultaneously lead to a larger BM term and less applicability of MLT.

Moving to the terms in the left column of Figure 8, we know based on the small sum of the residual and BM term that the ENTR, RAD, SUBS, and BASE-n-LAT terms collectively explain the actual evolution of the LWP_c very well until early afternoon. In particular, we can infer from the small sum of the residual and BM term that the sum of these four terms captures
345 the reduction of LWP_c , most rapid for the hiDhiL category and least for the loDloL category, in the morning, as is evident in the time series of the actual LWP_c tendency.

The ENTR, RAD, and BASE-n-LAT terms are expected to be the leading terms simply based on their roles in the CV $\langle\theta_1\rangle$ and $\langle q_1\rangle$ budgets. By contrast with the results in Figure 6, the SUBS terms are less important relative to the ENTR term. This is because the dz_i/dt term in Eq. (19) is constant in the two versions of LWP_c budget but the $d\langle\theta_1\rangle/dt$ and $d\langle q_1\rangle/dt$ terms are
350 strongly affected by the depth over which the volume-integrated forcing is distributed.

The SUBS term has the smallest diurnal fluctuation among the four terms. As a result, one can infer that the net effect of the ENTR, RAD, and BASE-n-LAT terms would approximately follow the trend of the actual LWP_c tendency for each category. Among these three terms, the ENTR and RAD terms always begin to weaken right after sunrise. The BASE-n-LAT term remains near its maximum strength until 09:00 for the loDloL category, but it starts to weaken right after sunrise for the
355 other two categories. This delay is likely the signature of better coupling with the surface. Due to this delay, although the rate of ENTR weakening for the loDloL category is slower than for the hiDloL category, the combined negative effect from ENTR and BASE-n-LAT terms (pink dash-dotted lines) diminishes faster between sunrise and 09:40 for loDloL. Since the change in the RAD term from sunrise to between 09:00 and 10:00 is about the same between these two categories, the delayed decrease in the BASE-n-LAT term explains the slower LWP_c reduction for the loDloL category. The weakening of the BASE-n-LAT term
360 balances that of the ENTR term closely for the hiDhiL category and the net effect (the pink dash-dotted lines) only weakens very slowly. As a result, the line for the RAD term is nearly parallel to the line for the actual LWP_c tendency. Interestingly, when the actual LWP_c tendency becomes the most negative in the morning for the loDloL and hiDloL categories, its value is very close to the SUBS term, meaning the ENTR, RAD, and BASE-n-LAT terms sum to about zero. It is unclear whether this is by accident but this is different for the hiDhiL category, where the actual LWP_c tendency can be much more negative than
365 the SUBS term, driven by the dramatic change in the RAD term.



To summarize, applying the MLT to the CV achieves satisfactory closure for the LWP_c budget from nighttime to early afternoon. In the morning, the coupling to the surface, evident in the BASE-n-LAT term, explains the relatively smaller loss of LWP_c for the loDloL category. The strong reduction of the RAD cooling causes the rapid reduction of LWP_c for the hiDhiL category. In the next section, we will use the budget analysis to understand the evolution of individual LES ensemble members, not just the mean evolution by category.

5 Nighttime and daytime evolution of LES ensemble members

With the categorization of cases and the budget analysis presented, we can now examine the nighttime and daytime evolution of simulations in detail.

5.1 Nighttime evolution of individual cases

Figure 9 highlights several aspects of the nighttime evolution. Overall, the nighttime evolution is characterized by the establishment of a positive correlation between LWP_c and a characteristic FT q_t . (Since subsidence is the only process that modifies the FT q_t profile in our simulations, the characteristic FT q_t is determined as follows. For a given time, we track the air mass at 20 m above z_i back in time using the subsidence profile, Eq. (1), to calculate its height at the beginning of the simulation, and represent the current FT q_t with the initial q_t at that height.) This can be seen by comparing the trajectories, colored by FT q_t , during the first three hours after the start of the simulations (Figure 9a) and during the three hours before sunrise (Figure 9b). It is also evident in the time series of the correlation coefficient between LWP_c and FT q_t (Figure 9c). At the beginning of each simulation, LWP_c is determined by three of the six prescribed parameters: BL θ_1 , BL q_t , and h_{mix} . As a result of the random sampling of the initial conditions, it is largely uncorrelated with the FT q_t even after we exclude cases based on criteria described in Section 2. FT q_t acts as a boundary condition for the simulated clouds. It affects LWP_c by modulating entrainment drying and the downward longwave radiation reaching the cloud top, two effects that compete with each other (Eastman and Wood, 2018). Based on the way we specify FT q_t profiles, the FT humidity controlling the longwave radiation positively correlates with the FT humidity that is relevant to the entrainment. For example, a case with a dry FT in our ensemble would experience greater entrainment drying; at the same time, it experiences strong radiative cooling because the FT is more transparent to longwave radiation. Although this strong radiative cooling favors high LWP_c , it also drives the clouds to entrain more, potentially reducing LWP_c . The positive correlation between LWP_c and FT q_t in our simulations suggests that the entrainment effect dominates.

Figures 9d–f show the LWP_c velocity, defined as the ratio between LWP_c change and mean LWP_c over a period of time, for the three hours before sunrise in LWP_c-z_i , N_d-z_i , and N_d-LWP_c planes, where the locations of dots are based on states at sunrise. Most cases with LWP_c less than 60 g m^{-2} at sunrise gain LWP_c during the three hours before sunrise (Figures 9d and 9f). This qualitatively agrees with Hoffmann et al. (2020) and Glassmeier et al. (2021). However, the sign of the LWP_c velocity is mixed for cases with greater LWP_c , where only 56% cases are gaining LWP_c . Among these cases, there is a weak negative correlation between z_i and LWP_c velocity, i.e., shallower/deeper BLs tend to see increasing/decreasing LWP_c . When



projected onto the N_d - LWP_c plane (Figure 9f), cases with low LWP_c and low N_d mostly gain LWP_c , while cases losing LWP_c only occur under high LWP_c and high N_d conditions. To some extent, this is consistent with the findings in Hoffmann et al. (2020) and Glassmeier et al. (2021).

However, due to some potentially realistic yet complicated correlations among LWP_c , N_d , z_i , and FT_{q_t} , we cannot simply attribute the correlation between LWP_c velocity and N_d to N_d . First, there is a positive correlation between LWP_c and N_d because we focus on the non-precipitating conditions and high LWP_c cases are only possible if N_d is sufficiently high to suppress precipitation (Figure 9f). Second, due to the positive correlation between LWP_c and z_i (deeper z_i supporting higher LWP_c , Figure 9d), there is also a positive correlation between z_i and N_d (notice very few cases in the upper left corner of Figures 9e). Similarly, because of the positive correlation between LWP_c and FT_{q_t} (Figures 9b and 9c), there is a positive correlation between FT_{q_t} and N_d (not shown).

We examine the correlation between radiative cooling and LWP_c to assess the impacts of the positive correlation between FT_{q_t} and LWP_c on the LWP_c tendency (Figure 10). Recall that to calculate the RAD term for the LWP_c budgets, we first calculate the CV-integrated radiative heating rate, then assume it evenly distributes in the CV to calculate the RAD term for the CV $\langle\theta_1\rangle$ budget, and then use Eq. (19) to calculate the RAD term for the LWP_c . The CV-integrated radiative heating rate strongly depends on FT_{q_t} while the cloud-top temperature (approximated using the lowest temperature in the mean temperature profile for the CV) explains a small portion of its variance (i.e., lower cloud-top temperature associates with less integrated radiative cooling, Figure 10a). The sensitivity of the CV-integrated radiative heating rate to FT_{q_t} increases for FT_{q_t} below 3 g kg^{-1} . More than 90% of cases have LWP_c greater than 40 g m^{-2} at this time and the emissivity of these clouds should have saturated (Garrett et al., 2002; Petters et al., 2012). (Our integrated radiative heating rate with FT_{q_t} of 4.5 g kg^{-1} , the FT_{q_t} estimated from Figure 2 in Petters et al. (2012) is very close to the saturated cloud-integrated radiative heating for longwave radiation in their Figure 1.) However, the RAD contribution to the CV $\langle\theta_1\rangle$ budget strongly and positively correlates with LWP_c (filled circles in Figure 10b) due to correlation between LWP_c and $\langle q_t \rangle$ as well as the scaling by CV depth. Earlier, we showed that the MLT-based budget works well for the loDloL and hiDloL categories during the nighttime (Figure 6). One might argue that it is more appropriate to assume the CV-integrated radiative heating rate is distributed from the surface to z_i . This scaling reduces the slope but not the sign of the correlation between the scaled RAD term and LWP_c (hollow circles in Figure 10b). It is only when we use the CV-integrated radiative cooling rate scaled with z_i in Eq. (19) that we find a positive correlation between the scaled RAD term for LWP_c tendency and LWP_c (hollow circles in Figure 10c; compare with hollow circles in Figure 10b).

The ratio between the scaled RAD term for the LWP_c tendency and for the CV $\langle\theta_1\rangle$ tendency depends on Γ_1 , $\langle\rho_0\rangle$, cloud depth, and $dz_{cb}/d\langle\theta_1\rangle$. Both the positive correlations between the cloud depth and LWP_c , as discussed in Hoffmann et al. (2020), and between other prefactors and LWP_c (not shown) contribute to this change in the sign of the correlation. For the LWP_c velocity, the division by LWP_c itself further modifies the correlation and the slope between a budget term and LWP_c (Figure 10d). In summary, not only the FT_{q_t} but also the z_i , the coupling state, and other factors (e.g., the prefactors in Eq. 19) shape the correlation between the radiative contribution to LWP_c tendency or velocity and the LWP_c .

We show the behavior of other terms for the LWP_c tendency in Figure 11a. The BASE-n-LAT term positively contributes to the LWP_c tendency. It negatively correlates with LWP_c for greater LWP_c , but positively correlates with it for lower LWP_c , prob-



ably because cases with lower LWP_c at sunrise, mostly in the loDloL category, have weaker boundary layer circulation. The ENTR term negatively contributes to the LWP_c tendency. It positively correlates with LWP_c for greater LWP_c , but negatively
435 correlates with it for lower LWP_c . Compared with the RAD and BASE-n-LAT terms, this correlation suggests that, to the first order, the entrainment is determined by the driving force for the turbulence, e.g., the radiative cooling and the boundary layer circulation. The SUBS term negatively contributes to the LWP_c velocity and positively correlates with LWP_c . After scaling by z_i , the BASE-n-LAT, ENTR, and SUBS terms show a much tighter positive, negative, and negative correlation with LWP_c (Figure 11b).

440 5.2 Daytime evolution of individual cases

Figures 12a and 12b show the most distinct feature of the daytime evolution of the individual cases. More decoupled cases tend to lose LWP_c more rapidly between sunrise and 12:00. For cases with z_i greater than about 0.9 km, the positive correlation between LWP_c and z_i at sunrise (dots in Figure 9b) becomes negative by 12:00 (dots in Figure 12a). In the afternoon, the LWP_c recovers for most cases and a positive correlation between LWP_c and z_i is restored by the end of the simulation.

445 To understand the factors controlling the evolution of LWP_c in the LWP_c-z_i plane, we investigate the behavior of four groups of cases with different properties: (1) loDloL cases with LWP_c at sunrise between 75 and 90 $g\ m^{-2}$ (2) hiDloL cases with LWP_c at sunrise in the same range (hiDloL Group 1), (3) hiDloL cases with LWP_c at sunrise between 150 and 180 $g\ m^{-2}$ (hiDloL Group 2), and (4) hiDhiL cases with LWP_c at sunrise between 240 and 300 $g\ m^{-2}$. Comparing Figures 12c and 12d, all four groups develop negative slopes between LWP_c and z_i between sunrise and 09:40, the least negative for the loDloL group
450 and the most negative for the hiDhiL group. Figure 13a shows the LWP_c tendencies and budget terms for each case in these four groups. The mean LWP_c tendency between sunrise and 09:40 differs between groups, by z_i , and by degree of coupling. For example, the loss of the LWP_c is faster/slower for groups with higher/lower LWP_c at sunrise; within each group, cases with greater z_i tend to lose LWP_c faster; the hiDloL Group 1 loses LWP_c faster than the loDloL group. Across different z_i , the RAD term positively correlates with the actual LWP_c tendency and shows similar spread (Figure 13b). The variation of the
455 RAD term between groups is consistent with both the nighttime behavior of the RAD term (i.e., more positive RAD term for low LWP_c and low FT q_t , e.g., cases with higher z_i in the loDloL group and hiDloL Group 1; also see Figures 9b and 10c) and the anticipated greater absorption of shortwave radiation for cases with higher LWP_c (e.g., the hiDhiL group). Unfortunately, we do not have separate longwave and shortwave radiative output to quantify the relative importance of longwave cooling and shortwave warming at this point. The ENTR and BASE-n-LAT terms are larger in magnitude than the RAD term (Figures 13c and 13d). The SUBS term shows negative z_i -dependence with small differences between groups (Figure 13e). The sum of the
460 BM term and the residual is very small, compared with other terms and the actual LWP_c tendency (Figure 13f). Based on these results, it is reasonable to take the sum of the SUBS, the BM, the PRCP, and the residual terms as a baseline and investigate how much the RAD, the ENTR, and the BASE-n-LAT terms drive the actual LWP_c tendency to deviate from this baseline. Figures 13g and 13h shows the sum of the RAD, the ENTR, and the BASE-n-LAT terms as well as the sum of the ENTR
465 and the BASE-n-LAT terms. Combined with the RAD term in Figure 13b, we conclude that the differences in LWP_c tendency



between groups with different LWP_c at sunrise are more associated with the RAD term, and the other details derive from a subtle balance between the RAD, ENTR, and BASE-n-LAT terms.

6 Discussion

In this section, we discuss an uncertainty in our budget analysis method, and then address the role of the interactive surface
470 fluxes in the simulations.

6.1 Uncertainty in ENTR term for $\langle\theta_1\rangle$ and $\langle q_t\rangle$ budgets

As described earlier, we use the entrainment fluxes (i.e., $d\Phi/dt|_{\text{ENTR}}$) from the BL $\langle\theta_1\rangle$ and $\langle q_t\rangle$ budgets to calculate the ENTR term for the CV. However, because the cloudy region of a domain is more turbulent than the clear-sky region, one would expect a higher entrainment flux in the cloudy region than the domain-mean for partially cloudy scenes. Underestimating the
475 magnitude of entrainment fluxes for the CV budget will cause a compensating error in the BASE-n-LAT term because the latter holds the residual between the actual CV $\langle\theta_1\rangle$ and $\langle q_t\rangle$ tendencies and the sum of the other terms.

In this subsection, we resort to the jump-based method (Eq. (15)) to assess the potential bias in our ENTR term. We first repeat the budget analysis for all clear-sky columns between the same base and top as the CV (denoted with “nCV”, meaning “not CV”), and then partition the total entrainment warming and drying in the CV and the nCV with the cloudy region jump
480 $\Delta\phi_{\text{CV}}$ and clear-sky jump $\Delta\phi_{\text{nCV}}$. This alternative estimate of the entrainment tendency for the CV is

$$\left. \frac{d\langle\phi\rangle}{dt} \right|_{\text{ENTR,alt}} = \frac{f_c (d\langle\phi\rangle/dt|_{\text{ENTR}}) + (1 - f_c) (d\langle\phi\rangle_{\text{nCV}}/dt|_{\text{ENTR}})}{f_c + (1 - f_c)\Delta\phi_{\text{nCV}}/\Delta\phi_{\text{CV}}}, \quad (20)$$

where “alt” stands for “alternative” and, again, ϕ represents either θ_1 or q_t . The question becomes how to define z_+ and z_- separately for ϕ profiles averaged in the cloudy and clear-sky regions to calculate the jumps. We follow Yamaguchi et al. (2011), where the authors check the domain-wide liquid water static energy (s_1) variance profile and define z_+ and z_- as the
485 levels with s_1 variance falling to 5% of the peak value. This method works reasonably well for DYCOMS-II RF02, the case simulated in Yamaguchi et al. (2011). (See Appendix C in that work.) We apply a constant absolute s_1 variance threshold of 0.235 K² (5% of 4.7 K², the peak s_1 variance in Yamaguchi et al., 2011) to search for z_+ and z_- to qualitatively capture the idea that the jump is smaller when turbulence mixing is weaker (lower peak s_1 variance).

We take a few extra steps to handle potential outliers. We exclude all time steps with $f_c < 0.01$ (1.9% of all time steps) and
490 keep the entrainment tendencies with $f_c > 0.99$ unchanged. Sometimes, the peak s_1 variance of a profile (usually the clear-sky ones) is below 0.235 K² and no z_+ or z_- are identified. For this situation, we keep a data point if only $\Delta\phi_{\text{CV}}$ can be calculated (about 6.4% of all time steps) and set its $\Delta\phi_{\text{nCV}}$ to 0, which actually exaggerates the difference between the cloudy and clear-sky region. We exclude a data point if neither $\Delta\phi_{\text{CV}}$ nor $\Delta\phi_{\text{nCV}}$ can be calculated, which rarely occurs.

For all three categories, we find no significant difference between the current and the alternative ENTR terms until the
495 afternoon (Figure 14). These results certainly depend on details of our method, e.g., the value of the s_1 variance threshold.



However, without a more solid foundation for an alternative choice of the threshold, sensitivity tests would not provide more reliable quantification of the bias.

One other method is to partition the entrainment flux using Eq. (13), such that

$$\left. \frac{d\Phi}{dt} \right|_{\text{ENTR,alt}} = \frac{1}{f_c + (1 - f_c)(\rho_{0,e}\phi_e)_{\text{nCV}}/(\rho_{0,e}\phi_e)_{\text{CV}}} \left. \frac{d\Phi}{dt} \right|_{\text{ENTR}}. \quad (21)$$

500 If we use $\rho_0\phi$ at z_+ identified earlier as an estimate of $\rho_{0,e}\phi_e$, the resulting ENTR terms are even closer to our current estimates.

These results do not necessarily mean that our current ENTR term is accurate. They simply suggest that, the two alternative methods we test to introduce contrast between cloudy region and clear-sky entrainment produce limited “correction” to current ENTR estimates. While these results provide some confidence in the robustness of current ENTR estimates, it seems to be inconsistent with the argument that the cloudy region is more turbulent and thus should entrain more. We argue that this inconsistency is partially rooted in the assumption that the movement of z_i is the result of the entrainment and the subsidence (Eq. (4)). We find that the air is on average descending/ascending at speeds around a few mm s^{-1} near the mean z_i in the cloudy/clear-sky region, which are indeed at very similar heights, despite the mean updraft/downdraft for the bulk of BL in the cloudy/clear-sky region (Figure 14c). This is probably the signature of a mesoscale (instead of large-scale, e.g., the prescribed subsidence, which is horizontally uniform in the domain) mean circulation in the FT, similar to the one shown in Zhou and Bretherton (2019). (See their Figure 9.) In other words, the cloudy/clear-sky region is more/less turbulent, but there may be a mesoscale downdraft/updraft limiting/promoting the growth of z_i . With Eq. (4), the effect of this mesoscale mean air motion is lumped into the entrainment. This finding suggests that our current ENTR term should be interpreted as a *collective effect* of processes (other than the prescribed subsidence) that move the z_i .

6.2 Response of surface fluxes to entrainment

515 One of the motivations for this work is to consider the role of the surface fluxes in compensating entrainment warming and drying. In this subsection, we take an analytical approach to this problem.

Considering that the evolutions of both the SHF and LHF in our simulations are driven primarily by $(\theta_{\text{SST}} - \theta_{\text{air}})$ and $(q_{\text{sat}}(\text{SST}) - q_{v,\text{air}})$ and thus θ_{air} and $q_{v,\text{air}}$, we take the time-derivative on both sides of the two formulas in Eq. (3),

$$\frac{d\text{SHF}}{dt} \approx -C_T U \frac{d\theta_{\text{air}}}{dt}, \quad \frac{d\text{LHF}}{dt} \approx -C_q U \frac{dq_{v,\text{air}}}{dt}. \quad (22)$$

520 With a well-mixed BL, $d\theta_{\text{air}}/dt$ and $dq_{v,\text{air}}/dt$ on the right-hand sides of Eq. (22) should be close to the BL $\langle\theta_t\rangle$ and $\langle q_t\rangle$ tendencies. This assumption is supported by our simulations. To be specific, for time steps with small relative decoupling index ($\mathcal{D} < 1$), the SHF and LHF tendencies directly calculated from the time series of SHF and LHF agree well with those diagnosed using Eq. (22) by replacing $d\theta_{\text{air}}/dt$ and $dq_{v,\text{air}}/dt$ in that equation with the actual $d\langle\theta_t\rangle/dt$ and $d\langle q_t\rangle/dt$ (Figure 15a and 15b). Under these conditions ($\mathcal{D} < 1$), the response of SHF and LHF to entrainment warming and drying can be directly calculated

525 as

$$\left. \frac{d\text{SHF}}{dt} \right|_{\text{ENTR}} = -C_T U \left. \frac{d\langle\theta_t\rangle}{dt} \right|_{\text{ENTR}}, \quad \left. \frac{d\text{LHF}}{dt} \right|_{\text{ENTR}} = -C_q U \left. \frac{d\langle q_t\rangle}{dt} \right|_{\text{ENTR}}. \quad (23)$$



The magnitude of these responses is much greater than the actual SHF and LHF tendencies because entrainment is only one of the leading terms affecting θ_{air} and $q_{v,\text{air}}$ (Figure 15a and 15b).

From Eqs. (3) and (22), one can derive the time scale for the SHF to respond to changes in θ_{air} to be

$$530 \quad \tau_T \approx c_p \langle \rho_0 \rangle z_i / C_T U, \quad (24)$$

where c_p is the specific heat capacity. This formula is essentially the same as the surface flux component of the time scale in Eq. 1 in Bretherton et al. (2010) and based on Schubert et al. (1979b). With the data from our LES ensemble, τ_T ranges from 18 to 42 h with both mean and median around 30 h based on time steps with $\mathcal{D} < 1$. The time scales derived for the LHF to respond to changes in $q_{v,\text{air}}$ are similar to τ_T . In a hypothetical scenario when a shift in the BL temperature and moisture tendencies is initialized and dominated by enhanced entrainment warming and drying due to, e.g., aerosol perturbation, surface fluxes will not fully balance the additional warming and drying promptly. Assuming the changes in surface fluxes follow an exponential decay characterized by the aforementioned time scales, it takes about 1/3 of the time scale to offset about 15% of the additional warming and drying. To offset a more substantial portion, e.g., those reported by Chun et al. (2023), requires longer times or changes in C_T , C_q , or U .

540 Under more decoupled conditions ($\mathcal{D} > 2$), the actual SHF and LHF tendencies are quite different from those diagnosed from BL $\langle \theta_l \rangle$ and $\langle q_l \rangle$ tendencies (Figure 15c and 15d). The medians of the actual SHF tendencies are negative for most of the daytime and change to positive after 15 h. Those based on BL $\langle \theta_l \rangle$ tendencies could be $1.1 \text{ W m}^{-2} \text{ h}^{-1}$ and $2.0 \text{ W m}^{-2} \text{ h}^{-1}$ more negative than the actual tendencies for the hiDloL and hiDhiL categories, respectively. This is because the net warming of the BL, mainly from entrainment and radiation, occurs aloft and has little impact on θ_{air} , which only increases due to the relatively weak SHF (left column in Figure 5). The medians of the actual LHF tendencies are much more negative than those based on BL $\langle q_l \rangle$ tendencies. Here, entrainment drying in the upper part of BL should not be able to affect $q_{v,\text{air}}$ very much, due to decoupling. As a result, the LHF moistens the surface-based mixed-layer faster than if the BL is well-mixed, which leads to faster decrease in LHF.

To summarize, the SHF and LHF always respond to the net changes in θ_{air} and $q_{v,\text{air}}$, contributed by all processes. Under well-mixed conditions, the time scale governing this response is relatively long. As a result, although the response of SHF and LHF to entrainment warming and drying can be estimated, it takes time and changes in surface transfer (characterized by C_T , C_q , and U) to see a strong response. Under decoupled conditions, the SHF and LHF can more quickly bring θ_{air} and $q_{v,\text{air}}$ towards equilibrium with the surface, given the shallow surface-based mixed-layer and assuming other factors remain unchanged. Thus, both SHF and LHF would weaken over time. This picture is compatible with our results for the BL $\langle q_l \rangle$ budget, which is dominated by the ENTR and SURF terms (the right column in Figure 5). During the nighttime, there is no negative correlation between the ENTR and SURF terms, especially for the loDloL category, where the cases are more coupled towards sunrise. During the daytime, there is a negative correlation between these two terms but this can not be interpreted as the SURF term directly responding to the ENTR term due to decoupling.



7 Summary

560 In this work, we explore the impacts of diurnal cycles, free-tropospheric (FT) humidity values, and interactive surface fluxes on the cloud system evolution of non-precipitating marine stratocumuli by analyzing 245 cases in an LES ensemble generated by perturbing initial conditions.

We separate the cases into three categories with distinct behavior based on their relative decoupling index (D) at 09:40 and cloud liquid water paths (LWP_c) at sunrise: a loDloL category ($D \leq 1$), a hiDloL category ($D > 1$ and $LWP_c \leq 180 \text{ g m}^{-2}$,
565 the highest LWP_c for the loDloL category), and a hiDhiL category ($D > 1$ and $LWP_c > 180 \text{ g m}^{-2}$). Cases in the loDloL category are commonly associated with lower z_i . They start with the lowest LWP_c and cloud fraction (f_c) among the three categories and may not ever become overcast. However, on average, they also experience the least reduction in LWP_c and f_c during the daytime. Clouds in the hiDloL category occur in deeper BLs, start with more LWP_c , and tend to be overcast during the nighttime. On average, they experience dramatic LWP_c and f_c reductions during the day. These clouds tend to evolve into
570 a cumulus-rising-into-stratocumulus structure in the afternoon. Clouds in the hiDhiL category share many features with those in the hiDloL category but show different timing and amplitude of daytime LWP_c and f_c fluctuations. The diurnal cycles of LWP_c and f_c for three categories are closely related to the diurnal cycles of their coupling states.

We perform a budget analysis to understand the diurnal cycle of LWP_c by tracking the mean θ_1 and q_t budgets for the “cloud volume” (CV), a volume consisting of all cloudy columns between the first grid box base below the mean cloud base and z_i ,
575 and then applying the LWP budget equation (Eq. (19)) to the CV, assuming it is well-mixed. By focusing on the cloudy region of the cloud layer, this method closes the budget with a very small residual until early afternoon. In particular, it adequately captures the rapid LWP_c reduction in the morning for all categories. A delayed decrease in the positive contribution to LWP_c from the BASE-n-LAT term, a term that tracks the impacts of the processes associated with the interface between the CV and the rest of the BL (i.e., CV base and lateral sides), after sunrise explains the slower LWP_c reduction in the loDloL category
580 than in the hiDloL category. For the hiDhiL category, the strong decrease in the radiative (RAD) cooling results in the most rapid LWP_c reduction in this category.

The impact of a humid FT on the evolution of simulations during the nighttime is distinct. A positive correlation between FT q_t and LWP_c emerges and strengthens towards sunrise. Because the longwave emissivity of clouds is saturated in most cases, the FT q_t strongly affects the CV-integrated radiative heating rate. As a result, there is stronger radiative cooling for
585 cases with lower LWP_c through the correlation between the FT q_t and LWP_c . This illustrates how the covariability among state variables and cloud controlling factors modifies the distribution of LWP_c tendency in state variable spaces. During the daytime, clouds in deeper BLs lose LWP_c faster in the morning, again suggesting that state variables beyond LWP_c and N_d are necessary to understand the LWP_c tendency. A closer analysis reveals that the LWP_c tendency in the morning varies with the LWP_c at sunrise, z_i , and the degree of decoupling. A budget analysis for LWP_c shows that the subsidence term (SUBS) causes
590 a more negative LWP_c tendency at deeper z_i and this effect is similar for cases with different LWP_c at sunrise and degree of decoupling. The entrainment (ENTR) and BASE-n-LAT terms closely balance each other, and there is a weak dependence of the net effect on z_i . It is the RAD term that differentiates cases with similar z_i in terms of the LWP_c tendency.



We show that the surface flux fluctuations in our simulations are dominated by the evolution of the lowest model level air temperature (θ_{air}) and water vapor mixing ratio ($q_{\text{v,air}}$), not the surface wind speed used in the surface flux calculation (U) or the transfer coefficients (C_T and C_q). As a result, the surface flux response to entrainment depends on the entrainment's impacts on θ_{air} and $q_{\text{v,air}}$. Under well-mixed conditions, this time scale for this response to offset entrainment warming and drying is $\sim \mathcal{O}(30\text{ h})$, consistent with the timescale reported in Schubert et al. (1979a). Based on this finding, we estimate that it takes about 10 h for the surface fluxes to offset 15% of the changes in entrainment warming and drying, assuming no changes in transfer coefficients (C_T and C_q) or surface wind speed (U); the magnitude of this response can be calculated from MLT-based budget analysis. Under decoupled conditions, the surface fluxes do not respond directly to entrainment (by definition), although there could be a negative correlation between the time series of surface fluxes and entrainment.

We demonstrate the emergence of the correlations among environmental conditions and state variables as the clouds evolve. All these correlations project onto the correlations with N_d and need to be carefully considered when we distill the causality between N_d and variables like the LWP_c tendency or the LWP_c velocity. We pursue this task in Zhang et al. (2024).

605 **Appendix A: Constructing initial thermodynamic profiles**

In this appendix, we describe the method for (1) creating the upper air θ_1 and q_1 profiles and (2) connecting them with the initial BL θ_1 and q_1 profiles (described in Section 2) to construct the initial θ_1 and q_1 profiles.

To prepare for the upper air profiles, we generate ERA5-based climatological profiles in a few steps. First, we produce mean profiles from all ERA5 profiles in the Californian stratocumulus region (i.e., the 10° by 10° box between 20°N , 30°N , 120°W , and 130°W as defined in Klein and Hartmann, 1993) during April, May, and June (the months with highest stratocumulus cover in the region; Wood, 2012) from 2000 to 2011. Then, we search for the height with the maximum θ_1 gradient below 2 km and keep the mean profile segments between this height and 35.8 km, the top of the mean profiles.

When we connect the θ_1 climatological profile produced this way to the initial BL profiles, some simulations experience very rapid growth in the inversion base height (z_i) in the first few hours, suggesting that the θ_1 gradient across the inversion is too weak. To solve this issue, we prepare a transitional profile for θ_1 . We average the observed θ_1 profiles during the warm season legs of the MAGIC campaign after translating them vertically to line up at inversion bases and having their BL values subtracted at all heights. We keep the first 1.5 km of this mean profile above the inversion base.

To construct an initial θ_1 profile, we first translate the transitional profile so that its lowest point attaches to point right above the inversion base. Next, we scale the ERA5-based θ_1 climatological profile so that its lowest point attaches to the highest point of the transitional profile (now sitting at 1.5 km above h_{mix}) while its highest point stays fixed at 35.8 km. For an initial q_1 profile, we scale the ERA5-based q_1 climatological profile so that its lowest point directly attaches to the point right above the inversion base while its highest point stays fixed at 35.8 km. A constant surface pressure of 1018.52 mb, based on ERA5 climatology, is used for all initial profiles. See Figure A1 for an illustration.



625 *Code and data availability.* The System for Atmospheric Modeling (SAM) code is publicly available at <http://rossby.msrc.sunysb.edu/SAM.html>. The ERA5 data is archived at Copernicus Climate Change Service (C3S) Climate Data Store (CDS) (Hersbach et al., 2017). The MAGIC data is available via ARM Data Discovery (Atmospheric Radiation Measurement (ARM) user facility, 2012). Data for reproducing the results will be provided following acceptance.

630 *Author contributions.* GF, TY, and YC initiated this study. TY, FG, and YC designed the LES ensemble. TY kindly performed the simulations. YC analyzed the data and wrote the manuscript. All authors contributed throughout the study and provided comments on the manuscript.

Competing interests. At least one of the (co-)authors is a member of the editorial board of Atmospheric Chemistry and Physics. Other than this, the authors declare that they have no conflict of interests.

635 *Acknowledgements.* This study has been supported by the U.S. Department of Energy (DOE), Office of Science, Office of Biological and Environmental Research, Atmospheric System Research (ASR) program (Interagency Award Number 89243023SSC000114), the U.S. Department of Commerce (DOC), National Oceanic and Atmospheric Administration (NOAA), Climate Program Office, Earth's Radiation Budget (ERB) program (Award Number 03-01-07-001), and NOAA cooperative agreements (NA17OAR4320101 and NA22OAR4320151). FG acknowledges support from The Branco Weiss Fellowship - Society in Science, administered by ETH Zürich. The computational and storage resources are provided by the NOAA Research and Development High Performance Computing Program (<https://rdhpcs.noaa.gov>). We thank Marat Khairoutdinov for graciously providing the SAM model, Ryuji Yoshida for compiling the ERA5 climatology, and Jan Kazil
640 for insights regarding the budget analysis.



References

- Ackerman, A. S., Kirkpatrick, M. P., Stevens, D. E., and Toon, O. B.: The impact of humidity above stratiform clouds on indirect aerosol climate forcing, *Nature*, 432, 1014–1017, <https://doi.org/10.1038/nature03174>, 2004.
- Ackerman, A. S., vanZanten, M. C., Stevens, B., Savic-Jovicic, V., Bretherton, C. S., Chlond, A., Golaz, J.-C., Jiang, H., Khairoutdinov, M., Krueger, S. K., Lewellen, D. C., Lock, A., Moeng, C.-H., Nakamura, K., Petters, M. D., Snider, J. R., Weinbrecht, S., and Zulauf, M.: Large-eddy simulations of a drizzling, stratocumulus-topped marine boundary layer, *Monthly Weather Review*, 137, 1083–1110, <https://doi.org/10.1175/2008MWR2582.1>, 2009.
- Albrecht, B. A.: Aerosols, cloud microphysics, and fractional cloudiness, *Science*, 245, 1227–1230, <https://doi.org/10.1126/science.245.4923.1227>, 1989.
- Atmospheric Radiation Measurement (ARM) user facility: Balloon-Borne Sounding System (SONDEWNP), 2012-10-01 to 2013-10-03, ARM Mobile Facility (MAG) Los Angeles, CA to Honolulu, HI - container ship Horizon Spirit; AMF2 (M1), Compiled by Even Keeler, Ken Burk, and Jenni Kyrouac. ARM Data Center: Oak Ridge, Tennessee, USA., <https://doi.org/10.5439/1595321>, last accessed: September 19, 2022, 2012.
- Boers, R. and Mitchell, R. M.: Absorption feedback in stratocumulus clouds influence on cloud top albedo, *Tellus A: Dynamic Meteorology and Oceanography*, 46, 229, <https://doi.org/10.3402/tellusa.v46i3.15476>, 1994.
- Bretherton, C. S. and Wyant, M. C.: Moisture transport, lower-tropospheric stability, and decoupling of cloud-topped boundary layers, *Journal of the Atmospheric Sciences*, 54, 148–167, [https://doi.org/10.1175/1520-0469\(1997\)054<0148:MTLTA>2.0.CO;2](https://doi.org/10.1175/1520-0469(1997)054<0148:MTLTA>2.0.CO;2), 1997.
- Bretherton, C. S., Blossey, P. N., and Uchida, J.: Cloud droplet sedimentation, entrainment efficiency, and subtropical stratocumulus albedo, *Geophysical Research Letters*, 34, <https://doi.org/10.1029/2006GL027648>, 2007.
- Bretherton, C. S., Uchida, J., and Blossey, P. N.: Slow manifolds and multiple equilibria in stratocumulus-capped boundary layers, *Journal of Advances in Modeling Earth Systems*, 2, <https://doi.org/10.3894/JAMES.2010.2.14>, 2010.
- Bretherton, C. S., Blossey, P. N., and Jones, C. R.: Mechanisms of marine low cloud sensitivity to idealized climate perturbations: A single-LES exploration extending the CGILS cases, *Journal of Advances in Modeling Earth Systems*, 5, 316–337, <https://doi.org/10.1002/jame.20019>, 2013.
- Caldwell, P. and Bretherton, C. S.: Large eddy simulation of the diurnal cycle in Southeast Pacific stratocumulus, *Journal of the Atmospheric Sciences*, 66, 432–449, <https://doi.org/10.1175/2008JAS2785.1>, 2009.
- Chen, Y.-C., Xue, L., Lebo, Z. J., Wang, H., Rasmussen, R. M., and Seinfeld, J. H.: A comprehensive numerical study of aerosol-cloud-precipitation interactions in marine stratocumulus, *Atmospheric Chemistry and Physics*, 11, 9749–9769, <https://doi.org/10.5194/acp-11-9749-2011>, 2011.
- Chun, J.-Y., Wood, R., Blossey, P., and Doherty, S. J.: Microphysical, macrophysical, and radiative responses of subtropical marine clouds to aerosol injections, *Atmospheric Chemistry and Physics*, 23, 1345–1368, <https://doi.org/10.5194/acp-23-1345-2023>, 2023.
- Deardorff, J. W.: Stratocumulus-capped mixed layers derived from a three-dimensional model, *Boundary-Layer Meteorology*, 18, 495–527, <https://doi.org/10.1007/bf00119502>, 1980.
- Eastman, R. and Wood, R.: The competing effects of stability and humidity on subtropical stratocumulus entrainment and cloud evolution from a Lagrangian perspective, *Journal of the Atmospheric Sciences*, 75, 2563–2578, <https://doi.org/10.1175/JAS-D-18-0030.1>, 2018.
- Feingold, G., Walko, R. L., Stevens, B., and Cotton, W. R.: Simulations of marine stratocumulus using a new microphysical parameterization scheme, *Atmospheric Research*, 47–48, 505–528, [https://doi.org/10.1016/S0169-8095\(98\)00058-1](https://doi.org/10.1016/S0169-8095(98)00058-1), 1998.



- Feingold, G., McComiskey, A., Yamaguchi, T., Johnson, J. S., Carslaw, K. S., and Schmidt, K. S.: New approaches to quantifying aerosol influence on the cloud radiative effect, *Proceedings of the National Academy of Sciences*, 113, 5812–5819, <https://doi.org/10.1073/pnas.1514035112>, 2016.
- Feingold, G., Ghate, V. P., Russell, L. M., Blosssey, P., Cantrell, W., Christensen, M. W., Diamond, M. S., Gettelman, A., Glassmeier, F., Gryspeerdt, E., Haywood, J., Hoffmann, F., Kaul, C. M., Lebsock, M., McComiskey, A. C., McCoy, D. T., Ming, Y., Mülmenstädt, J., Possner, A., Prabhakaran, P., Quinn, P. K., Schmidt, K. S., Shaw, R. A., Singer, C. E., Sorooshian, A., Toll, V., Wan, J. S., Wood, R., Yang, F., Zhang, J., and Zheng, X.: Physical science research needed to evaluate the viability and risks of marine cloud brightening, *Science Advances*, 10, eadi8594, <https://doi.org/10.1126/sciadv.adi8594>, 2024.
- Garrett, T. J., Radke, L. F., and Hobbs, P. V.: Aerosol effects on cloud emissivity and surface longwave heating in the Arctic, *Journal of the Atmospheric Sciences*, 59, 769–778, [https://doi.org/10.1175/1520-0469\(2002\)059<0769:AEOCEA>2.0.CO;2](https://doi.org/10.1175/1520-0469(2002)059<0769:AEOCEA>2.0.CO;2), 2002.
- Ghonima, M. S., Norris, J. R., Heus, T., and Kleissl, J.: Reconciling and validating the cloud thickness and liquid water path tendencies proposed by R. Wood and J. J. van der Dussen et al., *Journal of the Atmospheric Sciences*, 72, 2033–2040, <https://doi.org/10.1175/jas-d-14-0287.1>, 2015.
- Glassmeier, F., Hoffmann, F., Johnson, J. S., Yamaguchi, T., Carslaw, K. S., and Feingold, G.: An emulator approach to stratocumulus susceptibility, *Atmospheric Chemistry and Physics*, 19, 10 191–10 203, <https://doi.org/10.5194/acp-19-10191-2019>, 2019.
- Glassmeier, F., Hoffmann, F., Johnson, J. S., Yamaguchi, T., Carslaw, K. S., and Feingold, G.: Aerosol-cloud-climate cooling overestimated by ship-track data, *Science*, 371, 485–489, <https://doi.org/10.1126/science.abd3980>, 2021.
- Gryspeerdt, E., Goren, T., Sourdeval, O., Quaas, J., Mülmenstädt, J., Dipu, S., Unglaub, C., Gettelman, A., and Christensen, M.: Constraining the aerosol influence on cloud liquid water path, *Atmospheric Chemistry and Physics*, 19, 5331–5347, <https://doi.org/10.5194/acp-19-5331-2019>, 2019.
- Gryspeerdt, E., Glassmeier, F., Feingold, G., Hoffmann, F., and Murray-Watson, R. J.: Observing short-timescale cloud development to constrain aerosol–cloud interactions, *Atmospheric Chemistry and Physics*, 22, 11 727–11 738, <https://doi.org/10.5194/acp-22-11727-2022>, 2022.
- Hersbach, H., Bell, B., Berrisford, P., Hirahara, S., Horányi, A., Muñoz Sabater, J., Nicolas, J., Peubey, C., Radu, R., Schepers, D., Simmons, A., Soci, C., Abdalla, S., Abellan, X., Balsamo, G., Bechtold, P., Biavati, G., Bidlot, J., Bonavita, M., De Chiara, G., Dahlgren, P., Dee, D., Diamantakis, M., Dragani, R., Flemming, J., Forbes, R., Fuentes, M., Geer, A., Haimberger, L., Healy, S., Hogan, R., Hólm, E., Janisková, M., Keeley, S., Laloyaux, P., Lopez, P., Lupu, C., Radnoti, G., de Rosnay, P., Rozum, I., Vamborg, F., Villaume, S., and Thépaut, J.-N.: Complete ERA5 from 1940: Fifth generation of ECMWF atmospheric reanalyses of the global climate, <https://doi.org/10.24381/cds.143582cf>, 2017.
- Hersbach, H., Bell, B., Berrisford, P., Hirahara, S., Horányi, A., Muñoz-Sabater, J., Nicolas, J., Peubey, C., Radu, R., Schepers, D., Simmons, A., Soci, C., Abdalla, S., Abellan, X., Balsamo, G., Bechtold, P., Biavati, G., Bidlot, J., Bonavita, M., Chiara, G. D., Dahlgren, P., Dee, D., Diamantakis, M., Dragani, R., Flemming, J., Forbes, R. M., Fuentes, M., Geer, A., Haimberger, L., Healy, S., Hogan, R. J., Hólm, E., Janisková, M., Keeley, S., Laloyaux, P., Lopez, P., Lupu, C., Radnoti, G., de Rosnay, P., Rozum, I., Vamborg, F., Villaume, S., and Thépaut, J.-N.: The ERA5 global reanalysis, *Quarterly Journal of the Royal Meteorological Society*, 146, 1999–2049, <https://doi.org/10.1002/qj.3803>, 2020.
- Hoffmann, F., Glassmeier, F., Yamaguchi, T., and Feingold, G.: Liquid water path steady states in stratocumulus: Insights from process-level emulation and mixed-layer theory, *Journal of the Atmospheric Sciences*, 77, 2203–2215, <https://doi.org/10.1175/JAS-D-19-0241.1>, 2020.



- 715 Hoffmann, F., Glassmeier, F., Yamaguchi, T., and Feingold, G.: On the roles of precipitation and entrainment in stratocumulus transitions between mesoscale states, *Journal of the Atmospheric Sciences*, 80, 2791–2803, <https://doi.org/10.1175/JAS-D-22-0268.1>, 2023.
- Iacono, M. J., Delamere, J. S., Mlawer, E. J., Shephard, M. W., Clough, S. A., and Collins, W. D.: Radiative forcing by long-lived greenhouse gases: Calculations with the AER radiative transfer models, *Journal of Geophysical Research*, 113, <https://doi.org/10.1029/2008jd009944>, 2008.
- 720 Jones, C. R., Bretherton, C. S., and Leon, D.: Coupled vs. decoupled boundary layers in VOCALS-REx, *Atmospheric Chemistry and Physics*, 11, 7143–7153, <https://doi.org/10.5194/acp-11-7143-2011>, 2011.
- Kazil, J., Wang, H., Feingold, G., Clarke, A. D., Snider, J. R., and Bandy, A. R.: Modeling chemical and aerosol processes in the transition from closed to open cells during VOCALS-REx, *Atmospheric Chemistry and Physics*, 11, 7491–7514, <https://doi.org/10.5194/acp-11-7491-2011>, 2011.
- 725 Kazil, J., Feingold, G., Wang, H., and Yamaguchi, T.: On the interaction between marine boundary layer cellular cloudiness and surface heat fluxes, *Atmospheric Chemistry and Physics*, 14, 61–79, <https://doi.org/10.5194/acp-14-61-2014>, 2014.
- Kazil, J., Feingold, G., and Yamaguchi, T.: Wind speed response of marine non-precipitating stratocumulus clouds over a diurnal cycle in cloud-system resolving simulations, *Atmospheric Chemistry and Physics*, 16, 5811–5839, <https://doi.org/10.5194/acp-16-5811-2016>, 2016.
- 730 Kazil, J., Yamaguchi, T., and Feingold, G.: Mesoscale organization, entrainment, and the properties of a closed-cell stratocumulus cloud, *Journal of Advances in Modeling Earth Systems*, 9, 2214–2229, <https://doi.org/10.1002/2017MS001072>, 2017.
- Kazil, J., Christensen, M. W., Abel, S. J., Yamaguchi, T., and Feingold, G.: Realism of Lagrangian large eddy simulations driven by reanalysis meteorology: Tracking a pocket of open cells under a biomass burning aerosol layer, *Journal of Advances in Modeling Earth Systems*, 13, e2021MS002664, <https://doi.org/10.1029/2021MS002664>, 2021.
- 735 Khairoutdinov, M. F. and Randall, D. A.: Cloud Resolving Modeling of the ARM Summer 1997 IOP: Model formulation, results, uncertainties, and sensitivities, *Journal of the Atmospheric Sciences*, 60, 607–625, [https://doi.org/10.1175/1520-0469\(2003\)060<0607:CRMOTA>2.0.CO;2](https://doi.org/10.1175/1520-0469(2003)060<0607:CRMOTA>2.0.CO;2), 2003.
- Klein, S. A. and Hartmann, D. L.: The seasonal cycle of low stratiform clouds, *Journal of Climate*, 6, 1587–1606, [https://doi.org/10.1175/1520-0442\(1993\)006<1587:TSCOLS>2.0.CO;2](https://doi.org/10.1175/1520-0442(1993)006<1587:TSCOLS>2.0.CO;2), 1993.
- 740 Latham, J.: Control of global warming?, *Nature*, 347, 339–340, <https://doi.org/10.1038/347339b0>, 1990.
- Lewis, E. R., Wiscombe, W. J., Albrecht, B. A., Bland, G. L., Flagg, C. N., Klein, S. A., Kollias, P., Mace, G., Reynolds, R. M., Schwartz, S. E., Siebesma, A. P., Teixeira, J., Wood, R., and Zhang, M.: MAGIC: Marine ARM GPCI investigation of clouds, Tech. Rep. DOE/SC-ARM-12-020, U.S. Department of Energy, last accessed: July 15, 2023, 2012.
- Lilly, D. K.: Models of cloud-topped mixed layers under a strong inversion, *Quarterly Journal of the Royal Meteorological Society*, 94, 292–309, <https://doi.org/10.1002/qj.49709440106>, 1968.
- 745 Manshausen, P., Watson-Parris, D., Christensen, M. W., Jalkanen, J.-P., and Stier, P.: Invisible ship tracks show large cloud sensitivity to aerosol, *Nature*, 610, 101–106, <https://doi.org/10.1038/s41586-022-05122-0>, 2022.
- Mlawer, E. J., Taubman, S. J., Brown, P. D., Iacono, M. J., and Clough, S. A.: Radiative transfer for inhomogeneous atmospheres: RRTM, a validated correlated-k model for the longwave, *Journal of Geophysical Research: Atmospheres*, 102, 16 663–16 682, <https://doi.org/10.1029/97JD00237>, 1997.
- Mülmenstädt, J. and Feingold, G.: The radiative forcing of aerosol–cloud interactions in liquid clouds: Wrestling and embracing uncertainty, *Current Climate Change Reports*, 4, 23–40, <https://doi.org/10.1007/s40641-018-0089-y>, 2018.



- Nicholls, S.: The dynamics of stratocumulus: aircraft observations and comparisons with a mixed layer model, *Quarterly Journal of the Royal Meteorological Society*, 110, 783–820, <https://doi.org/10.1002/qj.49711046603>, 1984.
- 755 Petters, J. L., Harrington, J. Y., and Clothiaux, E. E.: Radiative–dynamical feedbacks in low liquid water path stratiform clouds, *Journal of the Atmospheric Sciences*, 69, 1498–1512, <https://doi.org/10.1175/JAS-D-11-0169.1>, 2012.
- Pincus, R. and Baker, M. B.: Effect of precipitation on the albedo susceptibility of clouds in the marine boundary layer, *Nature*, 372, 250–252, <https://doi.org/10.1038/372250a0>, 1994.
- Possner, A., Wang, H., Wood, R., Caldeira, K., and Ackerman, T. P.: The efficacy of aerosol extendashcloud radiative perturbations from near-
760 surface emissions in deep open-cell stratocumuli, *Atmospheric Chemistry and Physics*, 18, 17 475–17 488, <https://doi.org/10.5194/acp-18-17475-2018>, 2018.
- Prabhakaran, P., Hoffmann, F., and Feingold, G.: Evaluation of pulse aerosol forcing on marine stratocumulus clouds in the context of marine cloud brightening, *Journal of the Atmospheric Sciences*, 80, 1585–1604, <https://doi.org/10.1175/JAS-D-22-0207.1>, 2023.
- Qiu, S., Zheng, X., Painemal, D., Terai, C. R., and Zhou, X.: Daytime variation in the aerosol indirect effect for warm marine boundary layer
765 clouds in the eastern North Atlantic, *Atmospheric Chemistry and Physics*, 24, 2913–2935, <https://doi.org/10.5194/acp-24-2913-2024>, 2024.
- Sandu, I., Brenguier, J.-L., Geoffroy, O., Thouron, O., and Masson, V.: Aerosol impacts on the diurnal cycle of marine stratocumulus, *Journal of the Atmospheric Sciences*, 65, 2705–2718, <https://doi.org/10.1175/2008JAS2451.1>, 2008.
- Schubert, W. H., Wakefield, J. S., Steiner, E. J., and Cox, S. K.: Marine stratocumulus convection. Part I: Governing equa-
770 tions and horizontally homogeneous solutions, *Journal of the Atmospheric Sciences*, 36, 1286–1307, [https://doi.org/10.1175/1520-0469\(1979\)036<1286:MSCPIG>2.0.CO;2](https://doi.org/10.1175/1520-0469(1979)036<1286:MSCPIG>2.0.CO;2), 1979a.
- Schubert, W. H., Wakefield, J. S., Steiner, E. J., and Cox, S. K.: Marine stratocumulus convection. Part II: Horizontally inhomogeneous solutions, *Journal of the Atmospheric Sciences*, 36, 1308–1324, [https://doi.org/10.1175/1520-0469\(1979\)036<1308:MSCPIH>2.0.CO;2](https://doi.org/10.1175/1520-0469(1979)036<1308:MSCPIH>2.0.CO;2), 1979b.
- 775 Smalley, K. M., Lebsock, M. D., and Eastman, R.: Diurnal patterns in the observed cloud liquid water path response to droplet number perturbations, *Geophysical Research Letters*, 51, <https://doi.org/10.1029/2023GL107323>, 2024.
- Stevens, B. and Feingold, G.: Untangling aerosol effects on clouds and precipitation in a buffered system, *Nature*, 461, 607–613, <https://doi.org/10.1038/nature08281>, 2009.
- Toll, V., Christensen, M., Quaas, J., and Bellouin, N.: Weak average liquid-cloud-water response to anthropogenic aerosols, *Nature*, 572,
780 51–55, <https://doi.org/10.1038/s41586-019-1423-9>, 2019.
- Turton, J. D. and Nicholls, S.: A study of the diurnal variation of stratocumulus using a multiple mixed layer model, *Quarterly Journal of the Royal Meteorological Society*, 113, 969–1009, <https://doi.org/10.1002/qj.49711347712>, 1987.
- Twomey, S.: Pollution and the planetary albedo, *Atmospheric Environment*, 8, 1251–1256, [https://doi.org/10.1016/0004-6981\(74\)90004-3](https://doi.org/10.1016/0004-6981(74)90004-3), 1974.
- 785 Twomey, S.: The influence of pollution on the shortwave albedo of clouds, *Journal of the Atmospheric Sciences*, 34, 1149–1152, [https://doi.org/10.1175/1520-0469\(1977\)034<1149:TIOPOP>2.0.CO;2](https://doi.org/10.1175/1520-0469(1977)034<1149:TIOPOP>2.0.CO;2), 1977.
- van der Dussen, J. J., de Roode, S. R., and Siebesma, A. P.: Factors controlling rapid stratocumulus cloud thinning, *Journal of the Atmospheric Sciences*, 71, 655–664, <https://doi.org/10.1175/JAS-D-13-0114.1>, 2014.
- Wall, C. J., Storelvmo, T., and Possner, A.: Global observations of aerosol indirect effects from marine liquid clouds, *Atmospheric Chemistry and Physics*, 23, 13 125–13 141, <https://doi.org/10.5194/acp-23-13125-2023>, 2023.
- 790



- Wang, H. and Feingold, G.: Modeling mesoscale cellular structures and drizzle in marine stratocumulus. Part II: The microphysics and dynamics of the boundary region between open and closed cells, *Journal of the Atmospheric Sciences*, 66, 3257–3275, <https://doi.org/10.1175/2009JAS3120.1>, 2009.
- 795 Wang, H., Feingold, G., Wood, R., and Kazil, J.: Modelling microphysical and meteorological controls on precipitation and cloud cellular structures in Southeast Pacific stratocumulus, *Atmospheric Chemistry and Physics*, 10, 6347–6362, <https://doi.org/10.5194/acp-10-6347-2010>, 2010.
- Wang, S., Wang, Q., and Feingold, G.: Turbulence, condensation, and liquid water transport in numerically simulated nonprecipitating stratocumulus clouds, *Journal of the Atmospheric Sciences*, 60, 262–278, [https://doi.org/10.1175/1520-0469\(2003\)060<0262:TCALWT>2.0.CO;2](https://doi.org/10.1175/1520-0469(2003)060<0262:TCALWT>2.0.CO;2), 2003.
- 800 Wood, R.: Cancellation of aerosol indirect effects in marine stratocumulus through cloud thinning, *Journal of the Atmospheric Sciences*, 64, 2657–2669, <https://doi.org/10.1175/JAS3942.1>, 2007.
- Wood, R.: Stratocumulus clouds, *Monthly Weather Review*, 140, 2373–2423, <https://doi.org/10.1175/MWR-D-11-00121.1>, 2012.
- Yamaguchi, T., Randall, D. A., and Khairoutdinov, M. F.: Cloud modeling tests of the ULTIMATE–MACHO scalar advection scheme, *Monthly Weather Review*, 139, 3248–3264, <https://doi.org/10.1175/MWR-D-10-05044.1>, 2011.
- 805 Yamaguchi, T., Feingold, G., Kazil, J., and McComiskey, A.: Stratocumulus to cumulus transition in the presence of elevated smoke layers, *Geophysical Research Letters*, 42, 10–478, <https://doi.org/10.1002/2015GL066544>, 2015.
- Yamaguchi, T., Feingold, G., and Kazil, J.: Stratocumulus to cumulus transition by drizzle, *Journal of Advances in Modeling Earth Systems*, 9, 2333–2349, <https://doi.org/10.1002/2017MS001104>, 2017.
- Yamaguchi, T., Feingold, G., and Kazil, J.: Aerosol-cloud interactions in trade wind cumulus clouds and the role of vertical wind shear, *Journal of Geophysical Research: Atmospheres*, 124, 12 244–12 261, <https://doi.org/10.1029/2019JD031073>, 2019.
- 810 Yuan, T., Song, H., Wood, R., Oreopoulos, L., Platnick, S., Wang, C., Yu, H., Meyer, K., and Wilcox, E.: Observational evidence of strong forcing from aerosol effect on low cloud coverage, *Science Advances*, 9, <https://doi.org/10.1126/sciadv.adh7716>, 2023.
- Zhang, J. and Feingold, G.: Distinct regional meteorological influences on low-cloud albedo susceptibility over global marine stratocumulus regions, *Atmospheric Chemistry and Physics*, 23, 1073–1090, <https://doi.org/10.5194/acp-23-1073-2023>, 2023.
- 815 Zhang, J., Zhou, X., Goren, T., and Feingold, G.: Albedo susceptibility of northeastern Pacific stratocumulus: The role of covarying meteorological conditions, *Atmospheric Chemistry and Physics*, 22, 861–880, <https://doi.org/10.5194/acp-22-861-2022>, 2022.
- Zhang, J., Chen, Y.-S., Yamaguchi, T., and Feingold, G.: Cloud water adjustments to aerosol perturbations are buffered by solar heating in non-precipitating marine stratocumuli, *EGUsphere*, 2024, 1–xx, 2024.
- Zhou, X. and Bretherton, C. S.: Simulation of mesoscale cellular convection in marine stratocumulus: 2. Nondrizzling conditions, *Journal of Advances in Modeling Earth Systems*, 11, 3–18, <https://doi.org/10.1029/2018MS001448>, 2019.
- 820 Zhou, X., Kollias, P., and Lewis, E. R.: Clouds, precipitation, and marine boundary layer structure during the MAGIC field campaign, *Journal of Climate*, 28, 2420–2442, <https://doi.org/10.1175/JCLI-D-14-00320.1>, 2015.

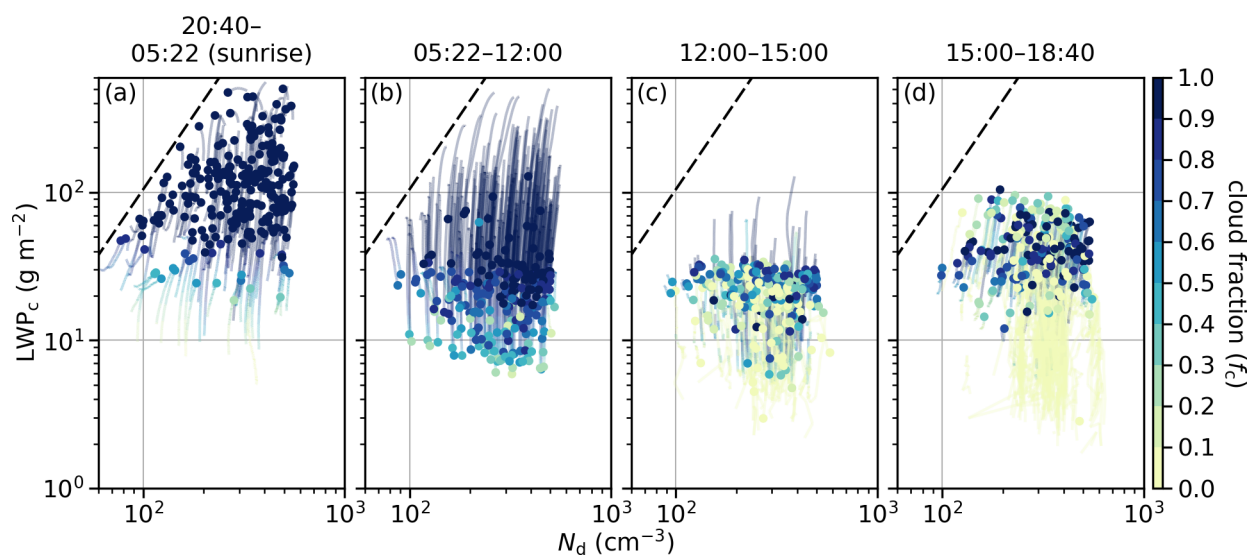


Figure 1. Evolution of the simulations in the plane of cloud droplet number concentration (N_d) and cloud LWP (LWP_c), split in to four time periods as shown in the panel titles. Curves indicate the trajectories over the time period and dots indicate the states at the end of the time period. The thick black dashed lines correspond to a characteristic mean drop radius of $12 \mu\text{m}$, below which precipitation is inhibited.

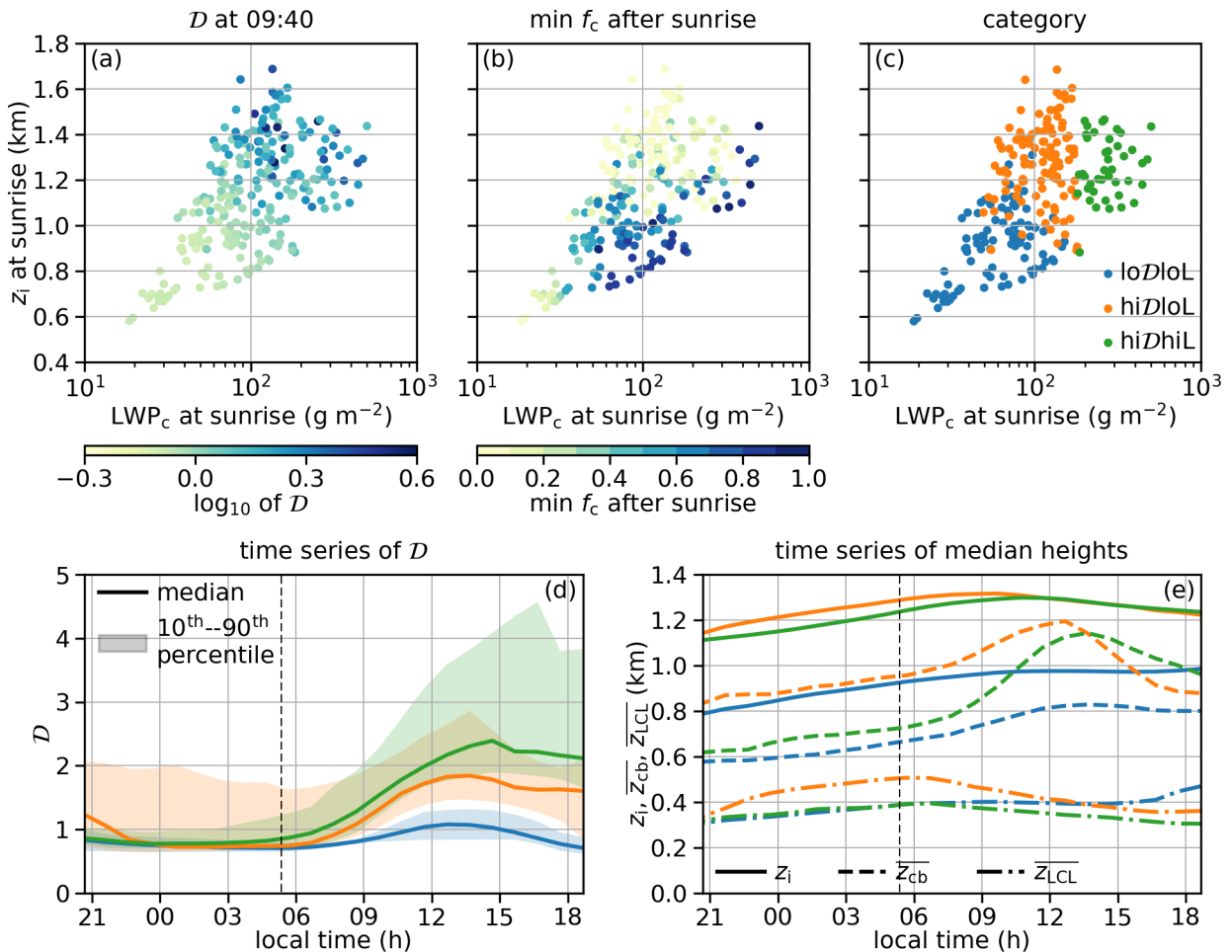


Figure 2. (a) Relative decoupling index (D) at 09:40 and (b) minimum cloud fraction ($\min f_c$) after sunrise in the plane of inversion base height (z_i) and cloud LWP (LWP_c) at sunrise; (c) categories based on D at 09:40 and LWP_c at sunrise: (1) loDloL ($D \leq 1$), (2) hiDloL ($D > 1$ and $LWP_c \leq 180\ g\ m^{-2}$), and (3) hiDhiL ($D > 1$ and $LWP_c > 180\ g\ m^{-2}$); time series of (d) median and quantiles of D and (e) medians of z_i , z_{cb} , and z_{LCL} by category. The vertical dashed grid lines in Panels (d) and (e) indicate sunrise.

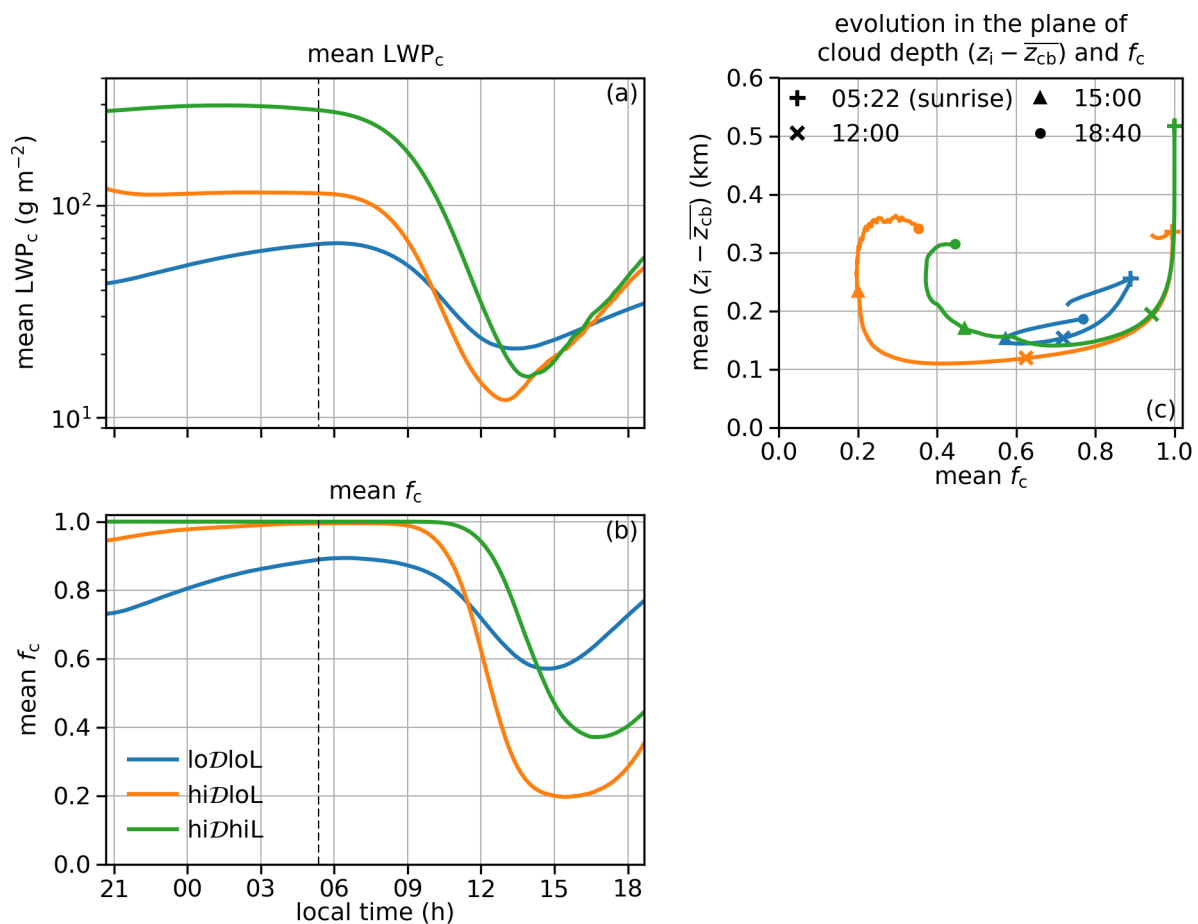


Figure 3. Time series of (a) mean cloud LWP (LWP_c), (b) mean cloud fraction (f_c); and (c) evolution by category in the plane of cloud depth ($z_i - \overline{z_{LCL}}$). The vertical dashed grid lines in Panels (a) and (b) indicate sunrise.

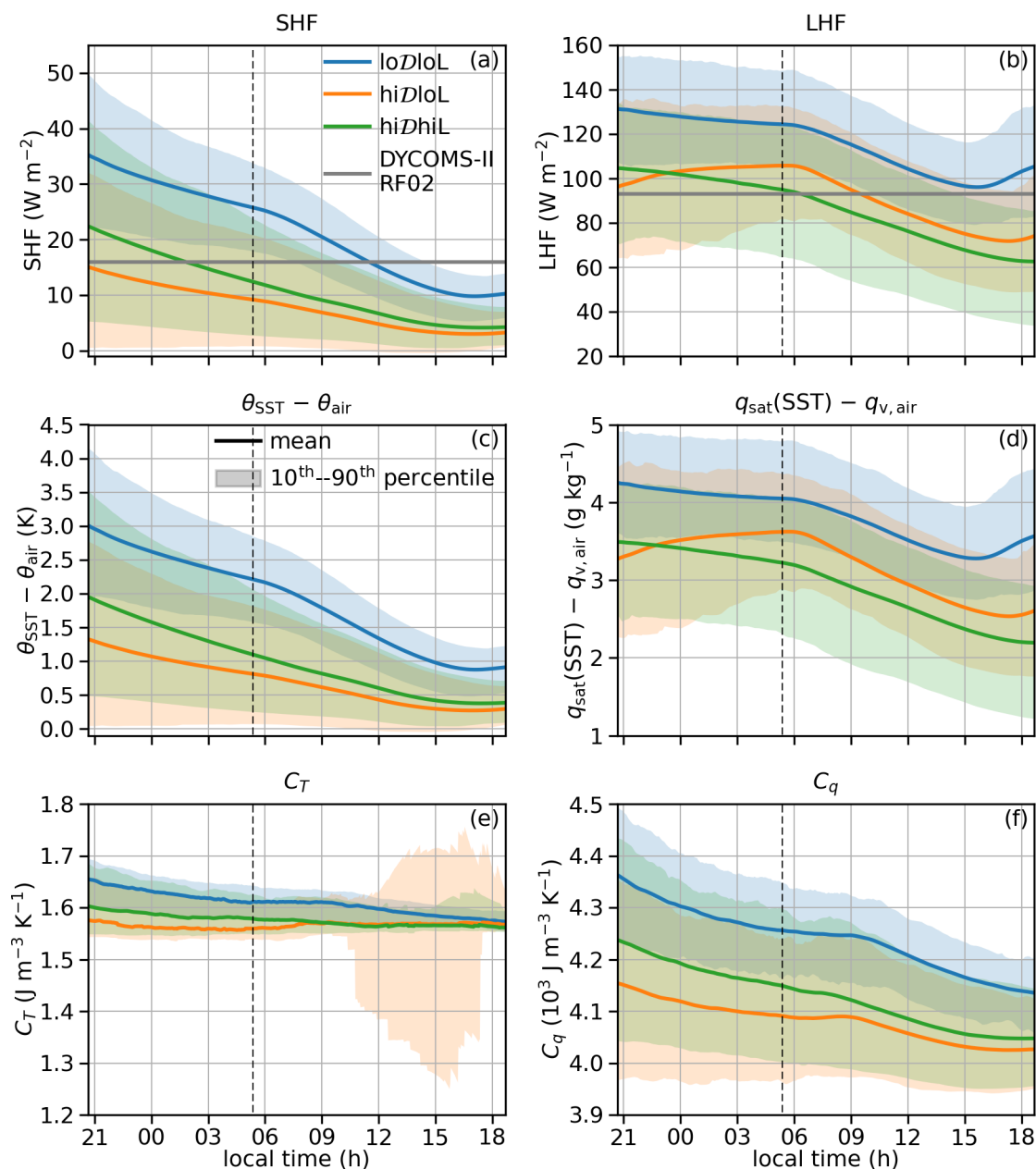


Figure 4. Time series of (a) surface sensible heat flux (SHF), (b) surface latent heat flux (LHF), (c) difference between potential temperature based on sea surface temperature (θ_{SST}) and lowest model level air potential temperature (θ_{air}), (d) difference between saturation mixing ratio at SST ($q_{sat}(SST)$) and lowest model level water vapor mixing ratio ($q_{v,air}$), (e) transfer coefficient for SHF (C_T), and (f) wind speed used for surface fluxes calculation (U) by category. The vertical dashed grid lines indicate sunrise.

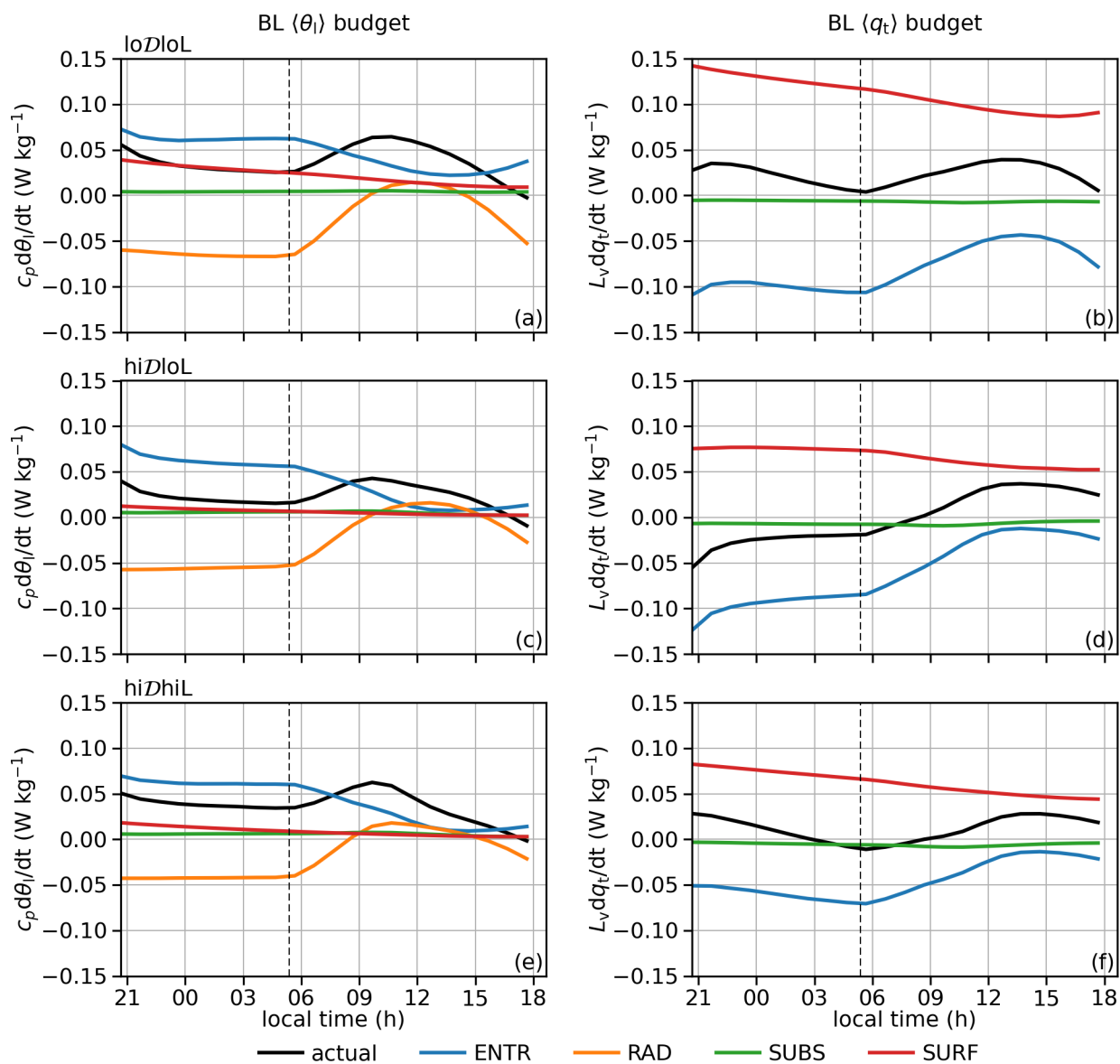


Figure 5. Time series of actual BL $\langle \theta_t \rangle$ and $\langle q_t \rangle$ tendencies and budget terms due to individual processes by category. The vertical dashed grid lines indicate sunrise.

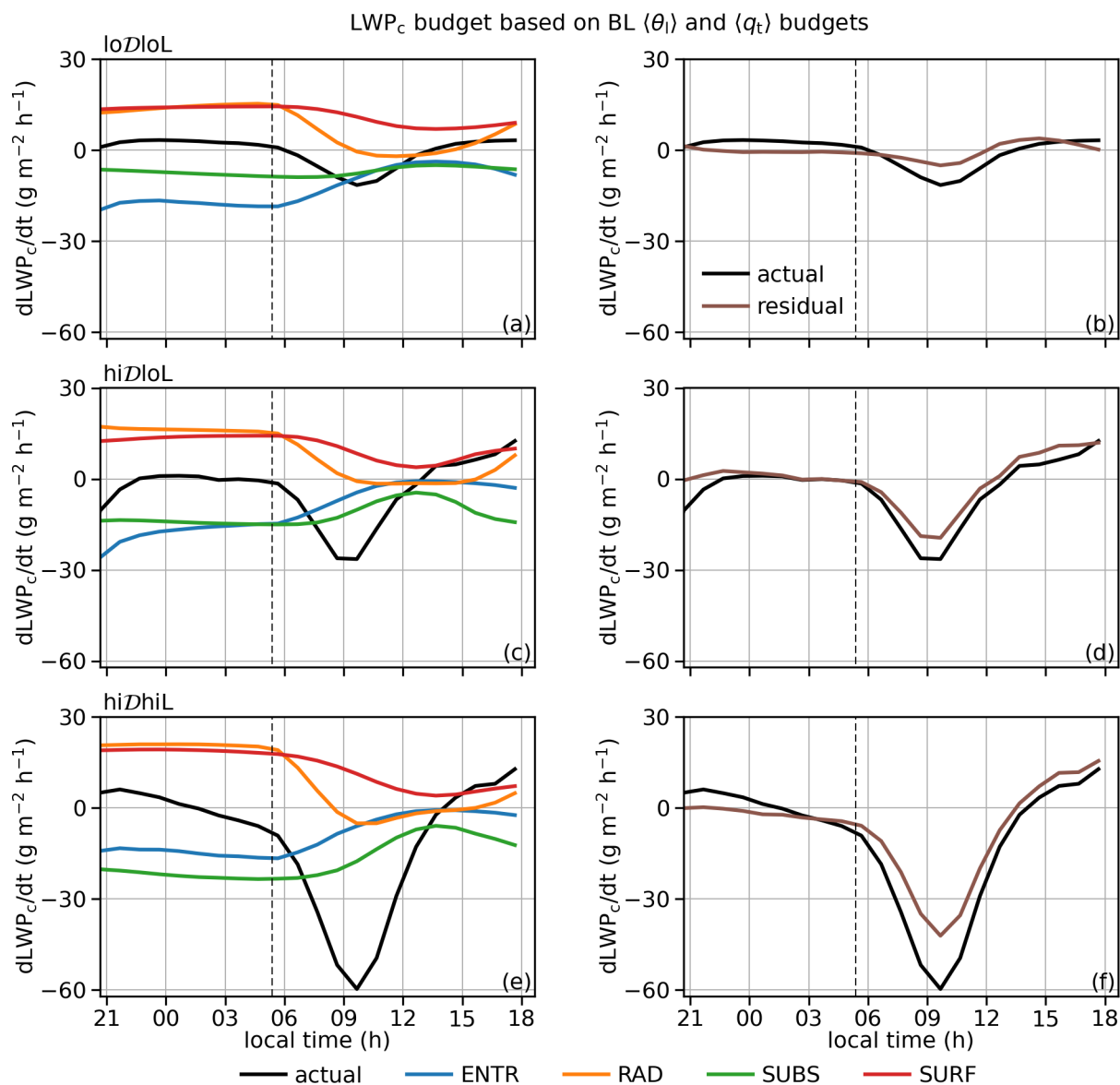


Figure 6. Time series of LWP_c tendencies and budget terms due to individual processes by category, based on BL $\langle \theta_l \rangle$ and $\langle q_l \rangle$ budgets. The actual LWP_c tendencies are shown in both the left and right columns for easier comparison with individual budget terms. The vertical dashed grid lines indicate sunrise.

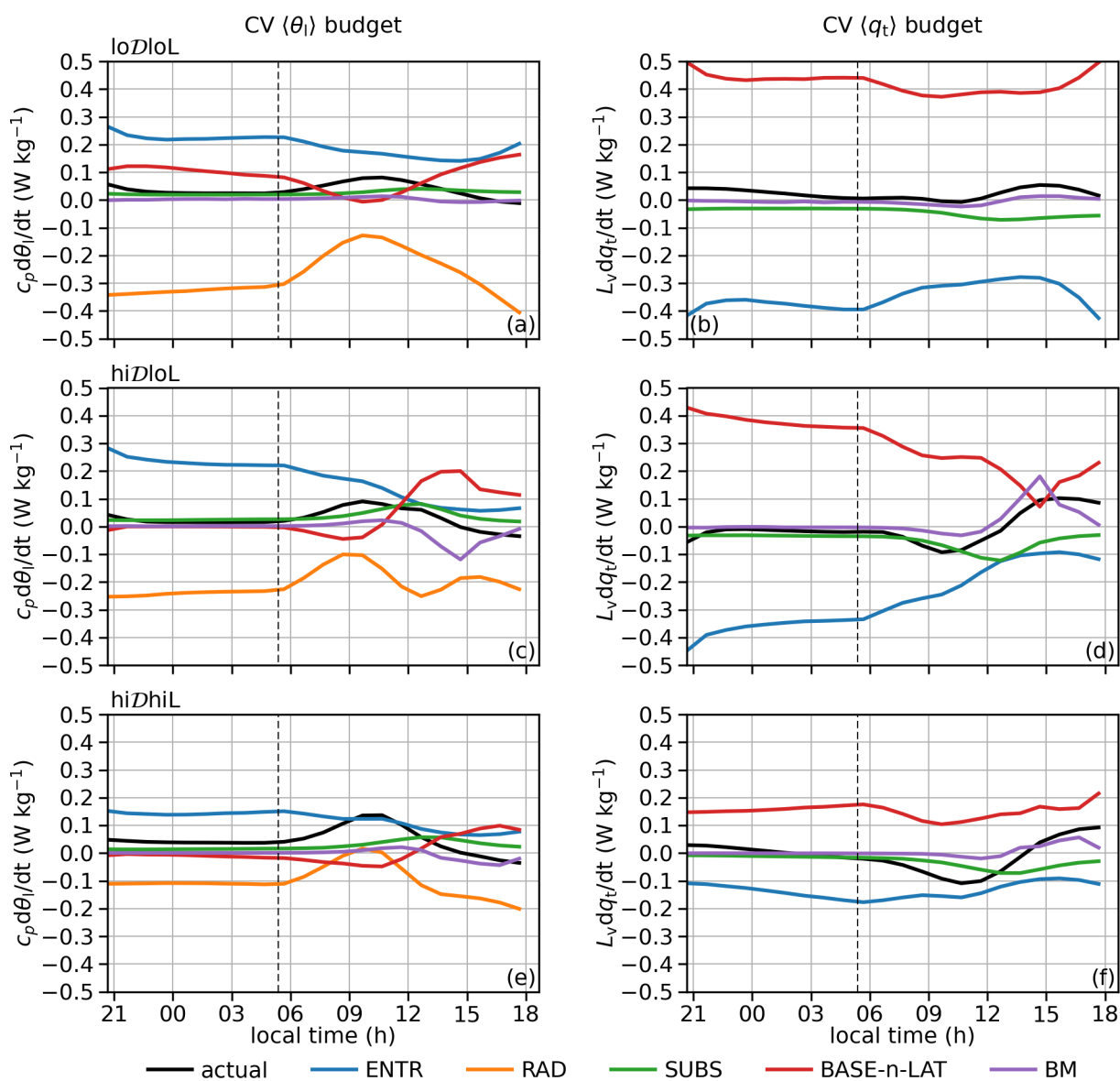


Figure 7. Time series of actual CV $\langle \theta_t \rangle$ and $\langle q_t \rangle$ tendencies and budget terms due to individual processes by category. The vertical dashed grid lines indicate sunrise.

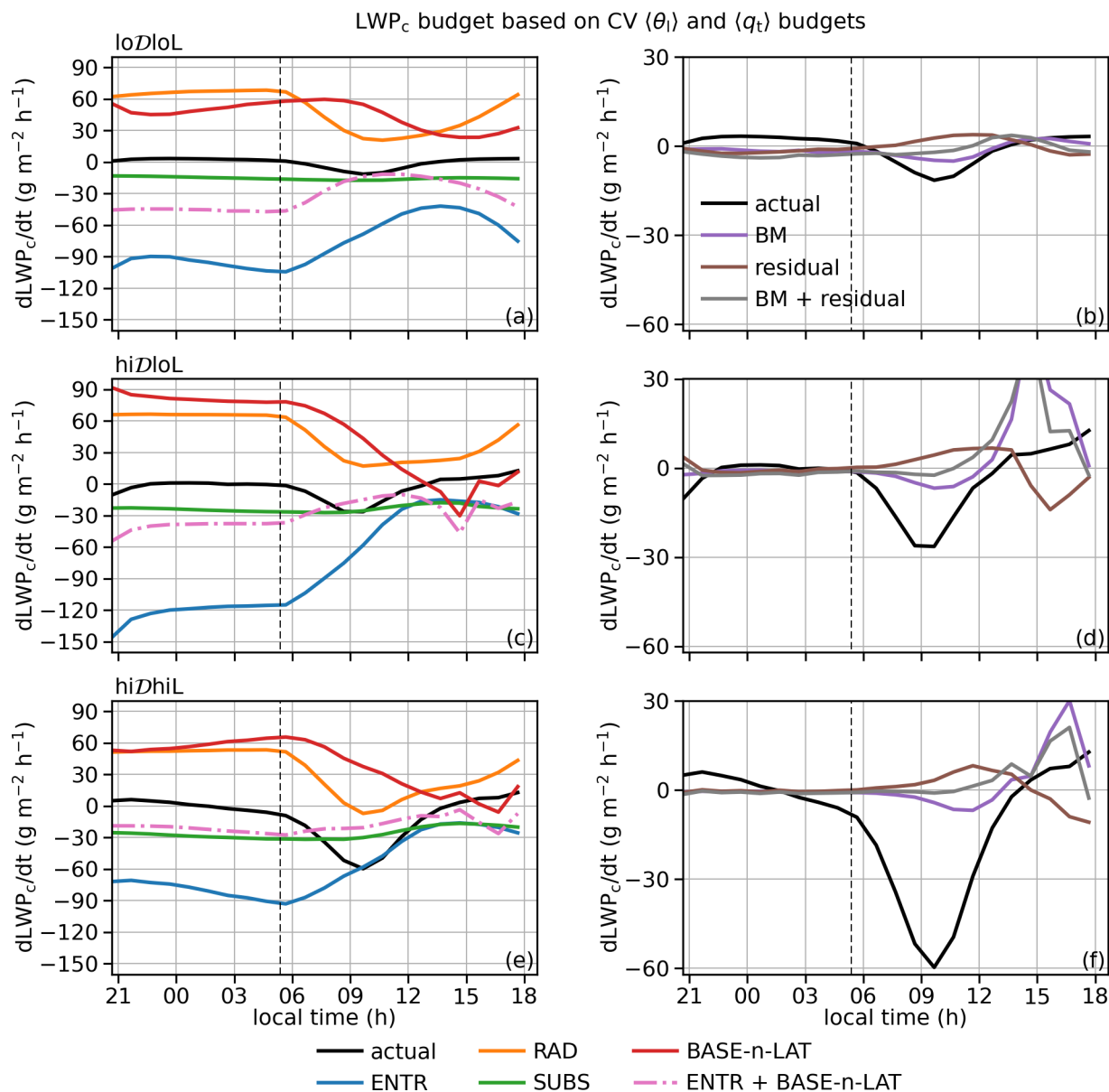


Figure 8. Time series of LWP_c tendencies and budget terms due to individual processes by category, based on CV $\langle\theta_t\rangle$ and $\langle q_t\rangle$ budgets. The actual LWP_c tendencies are shown in both the left and right columns for easier comparison with individual budget terms. The vertical dashed grid lines indicate sunrise.

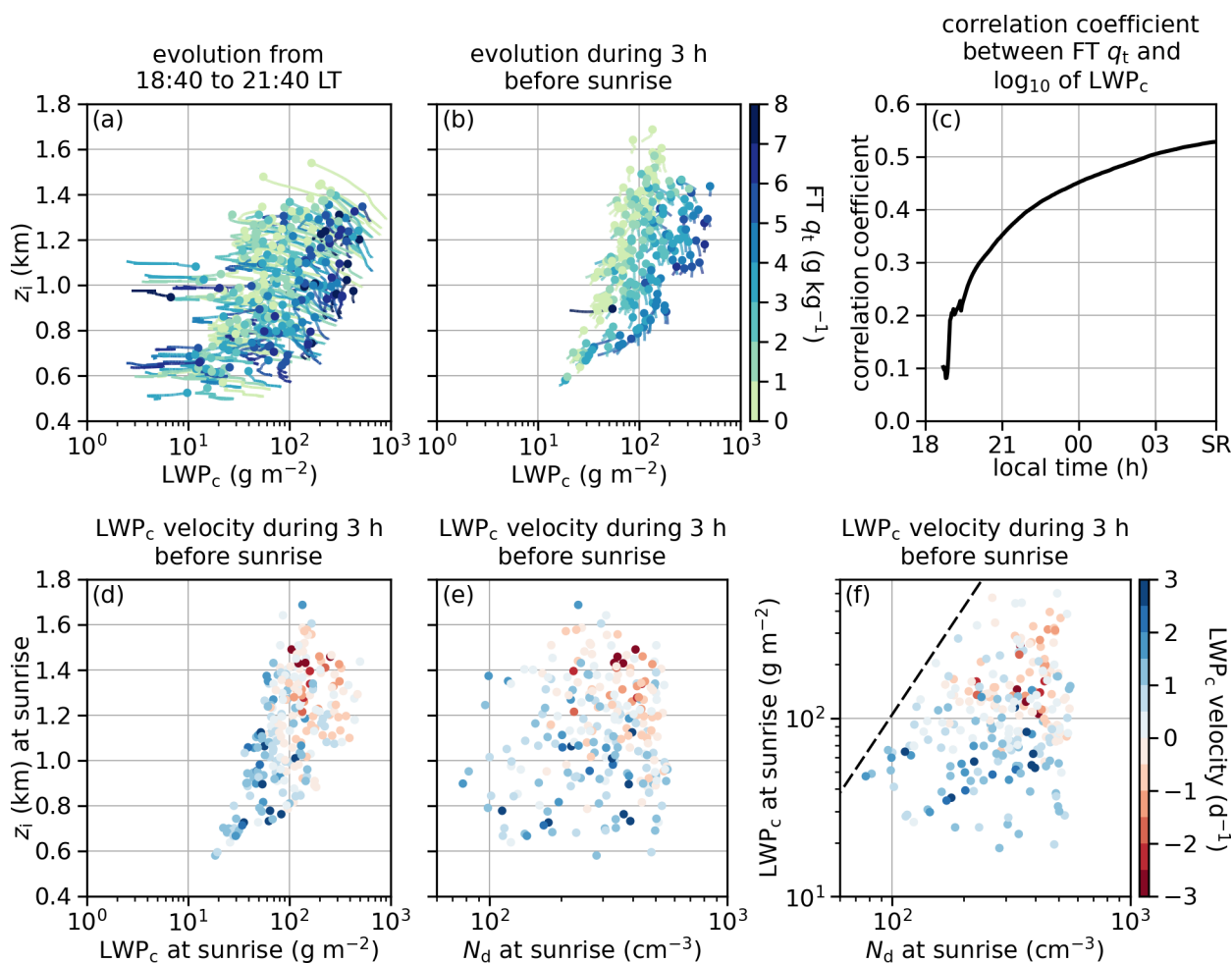


Figure 9. Evolution of LES ensemble members during nighttime. In Panels (a) and (b), curves indicate the trajectories over the time period, and dots indicate the states at the end of the time period shown in the panel titles. “SR” indicates sunrise.

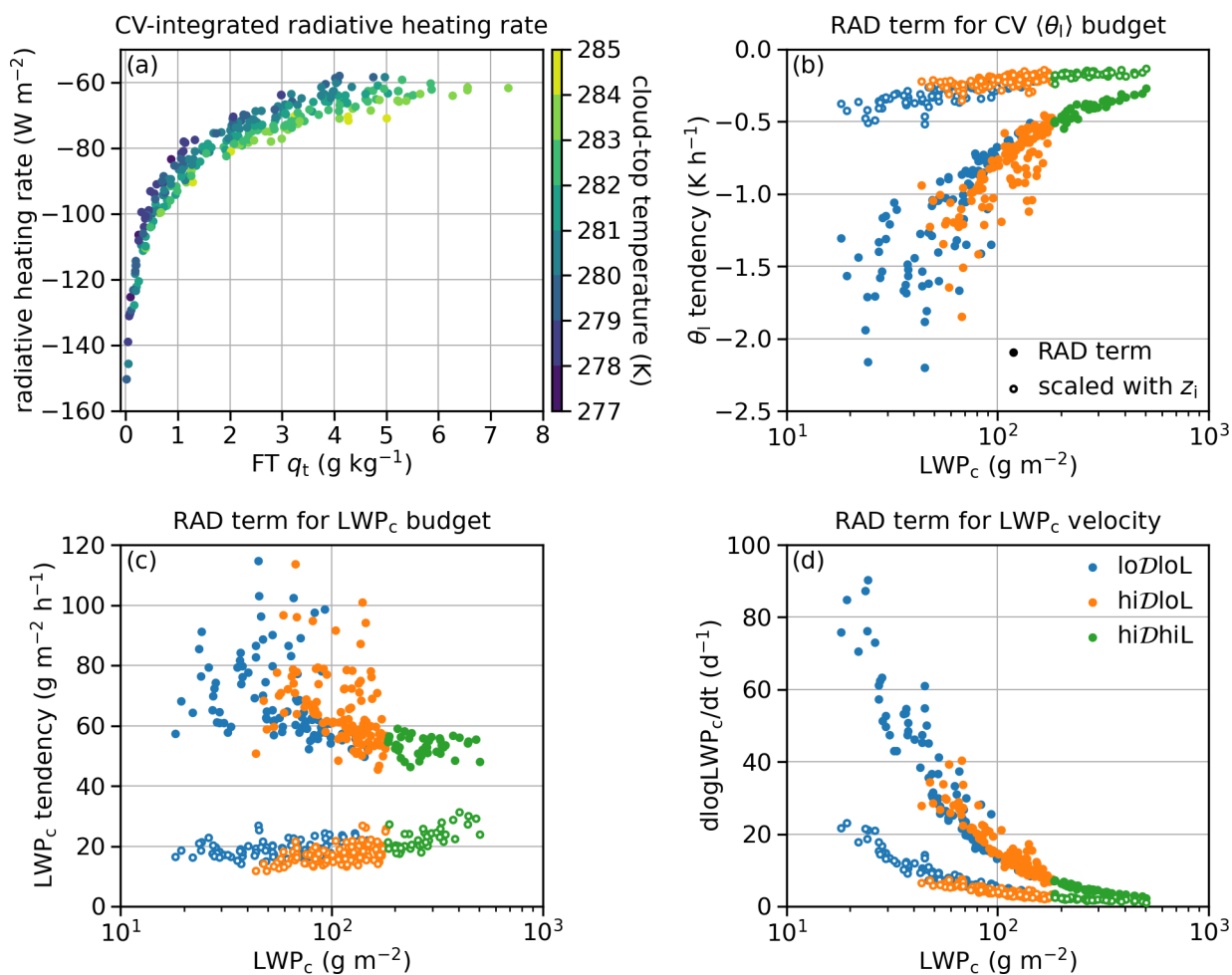


Figure 10. Radiative cooling at 04:40 LT. (a) CV-integrated radiative heating rate, (b) RAD term for CV $\langle \theta_1 \rangle$ budget, (c) RAD term for LWP_c budget, (d) radiative contribution to LWP_c velocity. Hollowed circles in Panels (b) and (c) represent the tendencies when the CV-integrated radiative heating rate is hypothetically uniformly distributed over the entire BL depth.

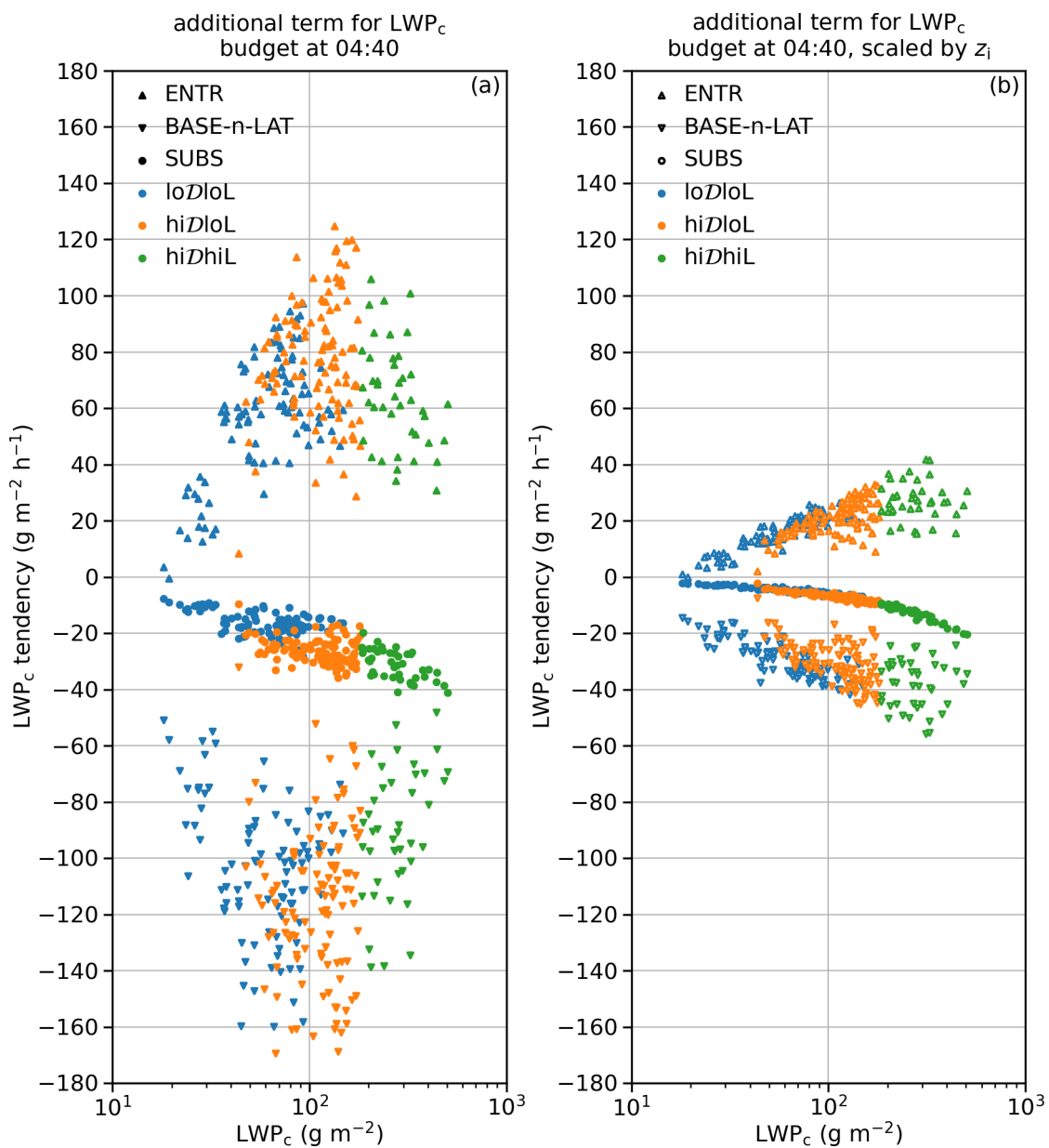


Figure 11. A few extra terms for LWP_c budget at 04:40 LT, in addition to the RAD term in Figure 10c.

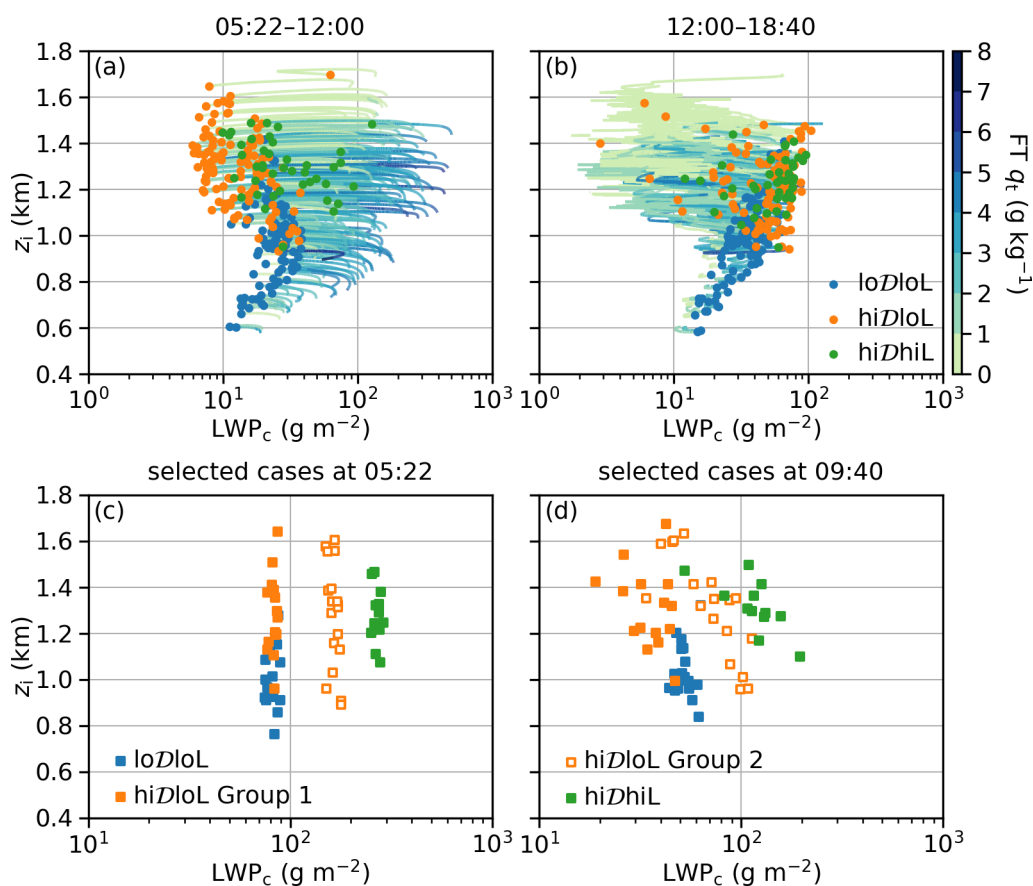


Figure 12. Evolution of LES ensemble members during daytime. In Panels (a) and (b), curves indicate the trajectories over the time period and dots indicate the states at the end of the time period, shown in the panel titles. Symbols in Panels (c) and (d) indicate groups of cases that are selected for further examination: (1) loDloL cases with LWP_c at sunrise between 75 and 90 g m^{-2} (2) hiDloL cases with LWP_c at sunrise in the same range (hiDloL Group 1), (3) hiDloL cases with LWP_c at sunrise between 150 and 180 g m^{-2} (hiDloL Group 2), and (4) hiDhiL cases with LWP_c at sunrise between 240 and 300 g m^{-2} .

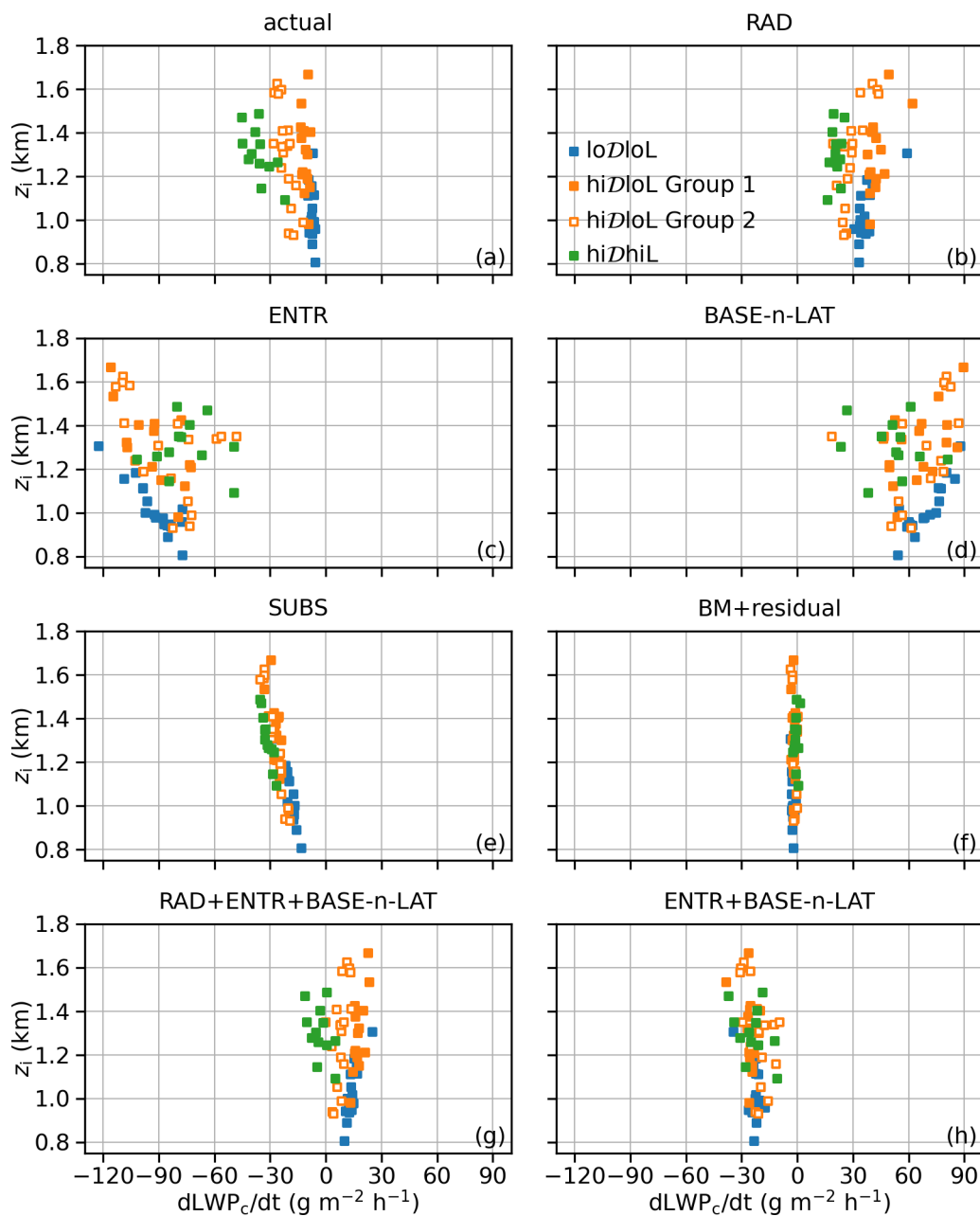


Figure 13. Mean LWP_c tendencies and budget terms due to individual processes for selected cases between sunrise and 09:40.

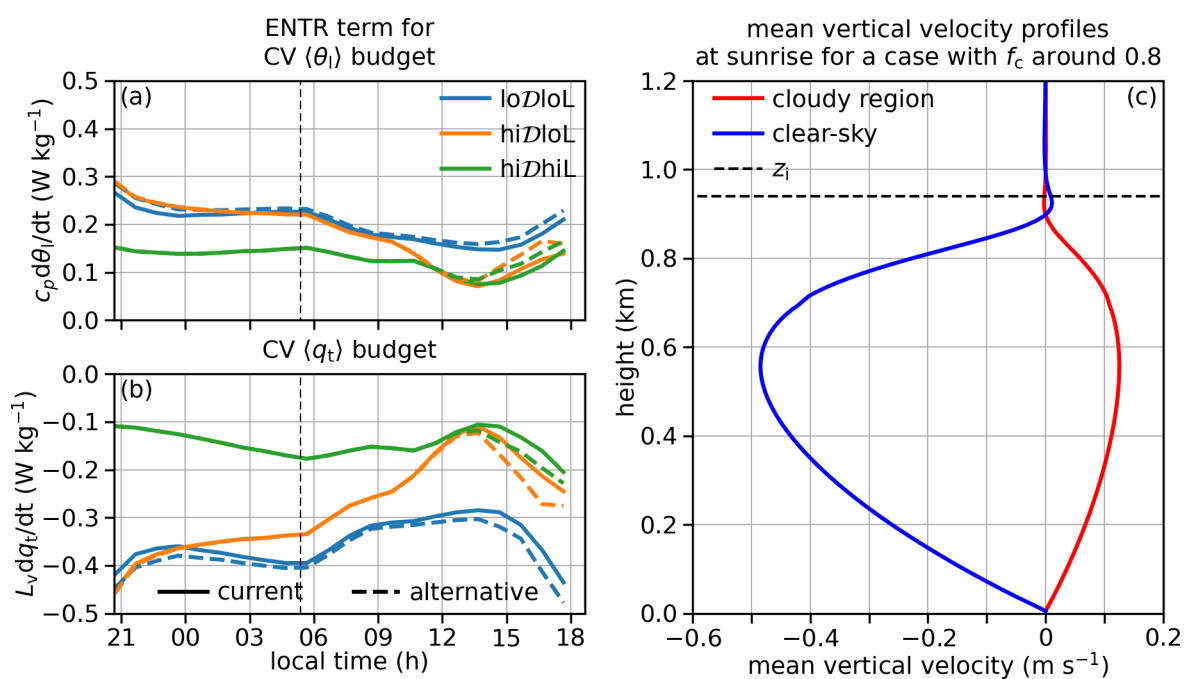


Figure 14. Time series of current and alternative estimates of the entrainment contribution to CV (a) $\langle \theta_t \rangle$ and (b) $\langle q_t \rangle$ budgets. The vertical dashed grid lines indicate sunrise. Panel (c) shows an example to facilitate the discussions near the end of Section 6.1.

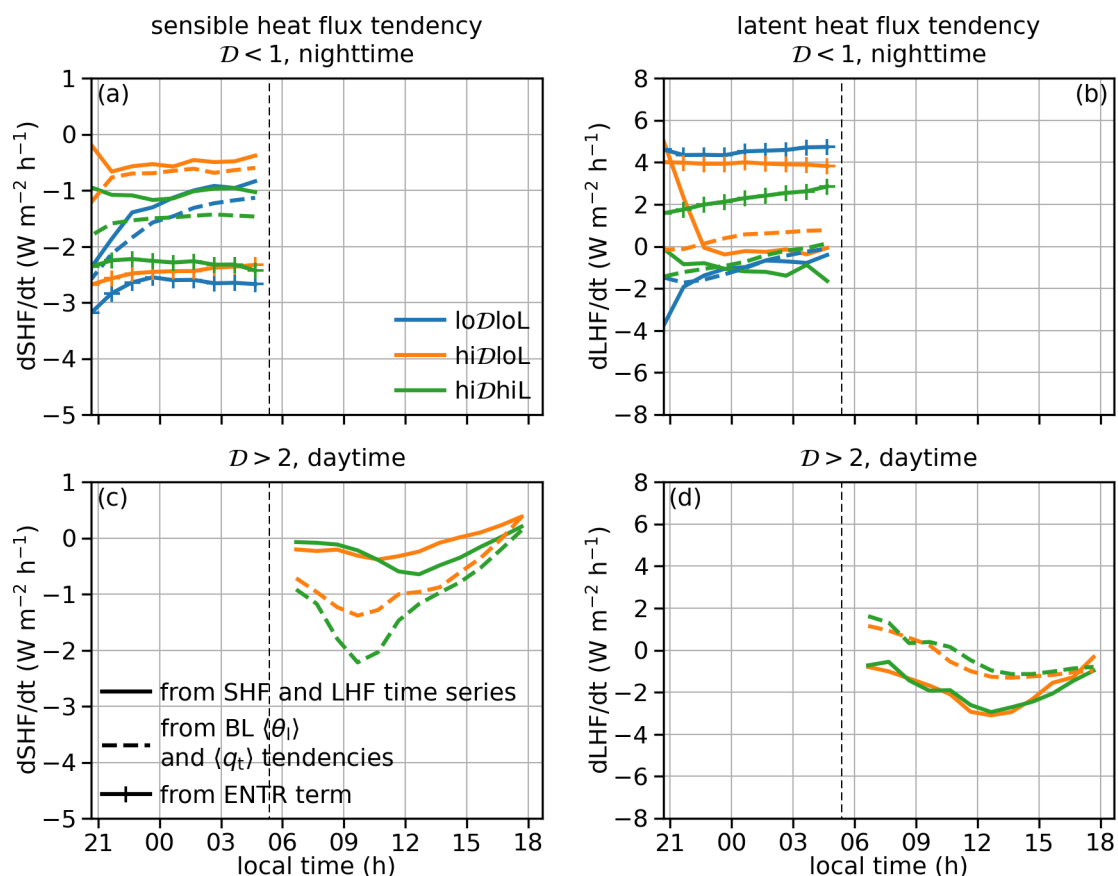


Figure 15. Time series of sensible heat flux (SHF, left column) and latent heat flux (LHF, right column) tendencies (1) directly from time series of SHF and LHF (solid lines), (2) calculated from actual BL $\langle \theta_l \rangle$ and $\langle q_t \rangle$ tendencies (dashed lines), and (3) contributed from the ENTR term for the BL $\langle \theta_l \rangle$ and $\langle q_t \rangle$ tendencies (solid lines with “+”) under more coupled condition (relative decoupling index (D) ≤ 1 , upper row) and more decoupled condition ($D > 2$, lower row). The vertical dashed grid lines indicate sunrise.

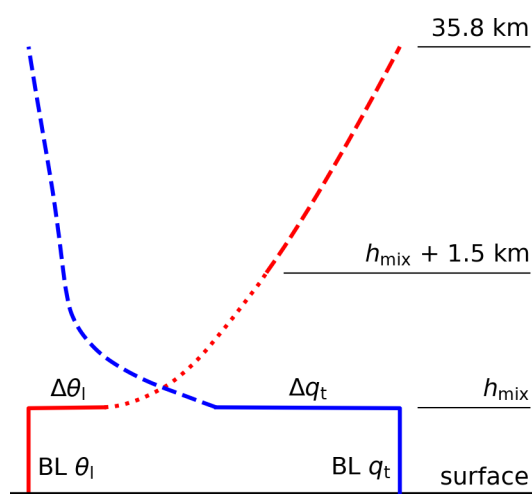


Figure A1. A sketch showing the construction of initial θ_1 and q_t profiles (in red and blue, respectively) from initial BL profiles (solid segments), ERA5-based climatological profiles (dashed segments) and the MAGIC-based transitional θ_1 profile (dotted segment).